On the radiation environment during consecutive balloon flights over New Mexico and Antarctica

Thomas Berger[1], Daniel Matthiä[1], Karel Marsalek[1], Bartos Przybyla[1], Joachim Aeckerlein[1], Markus Rohde[1], Michael Wirtz[1], Ralf Moeller[1], Leandro M. James[2], Michael A. Lane[2], Prital J. Johnson[2], Brian F. Rauch[3], Marianne B. Sowa[4], David J. Smith[4]

[1]German Aerospace Center (DLR), Institute of Aerospace Medicine, Cologne, Germany

[2]NASA Kennedy Space Center, Engineering Directorate, FL, USA

[3]Department of Physics and McDonnell Center for the Space Sciences, Washington University in St. Louis, MO, USA

[4]NASA Ames Research Center, Space Biosciences Division, CA, USA

Corresponding author: Thomas Berger (thomas.berger@dlr.de)

Key Points:

- Radiation dose values, fluence and energy distribution spectra were measured for two distinct stratospheric balloon flights
- Long duration balloon flight observations occurred over New Mexico (7 hours) and over Antarctica (28 days)
- The Regener maximum was identified and described for both missions

Abstract

Remarkably, we know more about the radiation environment onboard the International Space Station than we do about radiation values at altitudes between 30-40 km in the middle stratosphere. Within this work, we provide data about the radiation dose measured during two consecutive balloon flights flown within a 4-month timeframe over New Mexico and Antarctica. Data were measured with the M-42 radiation detector. On each flight, the M-42 was installed as part of a larger research payload: MARSBOx (New Mexico, 23 September 2019); and E-MIST (Antarctica, 15 December 2019-12 January 2020). The temporal proximity of the flights provided similar prevailing space weather conditions and solar activity (minimal during each mission). Against that common backdrop, the main differences between flights, including mission duration and geomagnetic shielding could be readily compared. Near identical space weather conditions provided a window of opportunity for studying the influence of altitude and geomagnetic shielding on dose and fluence rate of galactic cosmic radiation under maximum intensity conditions. Herein, we report relevant count- and dose rates for the missions, alongside Geant4 Monte Carlo calculations; this included crossings of the Regener maximum during the ascent and descent flights over New Mexico and the absence of a distinct maximum in dose rates at zero geomagnetic shielding for the polar flight. While dose rates in silicon at float altitudes (≈35 km-39 km) were a maximum of 2.5±0.4 µGy/h over New Mexico, we reached values of up to 8.4±0.3 µGy/h over Antarctica, thereby approaching dose rates similar to the surface of Mars.

Plain Language Summary

The radiation environment during two high altitude balloon missions was measured with the German Aerospace Center M-42 radiation detector. These missions were successfully executed in September 2019 over New Mexico (MARSBOx) and in December 2019 and January 2020 over Antarctica (E-MIST) with a collaboration between NASA and DLR. Considering the missions were flown at similar, near solar minimum conditions, we could readily draw comparisons of the radiation environment at two distinct locations in Earth's middle stratosphere (polar and mid-latitude profiles).

1. Introduction

The Space radiation environment has been extensively studied, even at inaccessible locations, including at high altitudes where aircraft travel, in low Earth orbit (LEO) onboard the International Space Station (ISS) (Berger et al., 2020), and, more recently, on the surface of other planetary bodies such as the Moon (Zhang et al., 2020) and Mars (Zeitlin et al., 2019; Berger et al., 2020). The components of the radiation environment in deep space result from galactic cosmic radiation (GCR) and sporadic solar particle events (SPEs). However, when considering the radiation environment at LEO altitudes – applicable to a spacecraft like the ISS – charged particles trapped inside the radiation belts must also be accounted for in measurements and models. Due to mass shielding (effective against the electrons in the outer radiation belt), the most relevant radiation belt contribution to the radiation exposure of astronauts inside the ISS is derived from trapped protons in the South Atlantic Anomaly (SAA). Measuring radiation doses for commercial aircraft traveling through the tropopause/lower stratosphere (~10 km – 12 km) is a similarly complex exercise due to GCR scattering into the atmosphere, creating a mixed radiation field of primary and secondary particles (with a high contribution from electrons and neutrons). Due to numerous radiation measurements in the regions where commercial aircraft and human spacecraft regularly travel, these environments can now be quite reliably characterized and described. Yet the same is not true for a wide zone of our Earth's middle stratosphere, around 20 – 40 km, which to this day remains essentially uncharted territory for fundamental dose rate measurements. To date, information characterizing the radiation field in this region of the atmosphere has been built upon only a handful of scientific balloon measurements.

Considering exposure to GCR is a major, unresolved risk for human spaceflight, we note the potential utility of using the Earth's stratosphere for establishing a natural testbed to study the influence of mass and geomagnetic shielding on dose. For instance, shielding conditions in space cannot be realistically changed to perform such systematic studies, but changing altitude (air pressure) during a balloon flight into the stratosphere can quantify the mass shielding parameter quite precisely. Measurements on balloons introduce atmospheric shielding between approximately 1000 g/cm^2 and a few g/cm^2. If utilizing the full range of the dynamic proxy, teams could conceivably draw comparisons with conditions encountered in a spacecraft like the ISS (i.e., lowest mass shielding); or conditions expected on other planets with comparable atmospheric densities (i.e., higher mass shielding). Thus, additional data from the Earth's stratosphere will be valuable for benchmarking models that calculate the exposure from cosmic radiation for a variety of imminent space exploration scenarios. In the 1930s it was discovered that the intensity of primary and secondary particles of cosmic radiation as measured by ionization rates at a given altitude can go through a maximum (Regener & Pfotzer, 1935). Based

on the work by Carlson & Watson (2014), this ionization phenomenon, is now denoted as the *Regener-maximum*, and the altitude where the maximum occurs depends on the specific boundary conditions.

In the decades following this discovery, the ionization rates in the atmosphere were studied extensively as a function of altitude (Carmichael & Dymond, 1939; Lowder & Beck, 1966; Lowder et al., 1972; Neher, 1958, 1971; Rosen et al., 1985). The variation of these profiles caused by solar modulation at high geomagnetic latitudes was comprehensively investigated by Neher (1971) and it was shown that the ionization rate did not form a maximum at high latitudes during solar minimum conditions. Later, detailed studies of individual particle species followed, such as electrons (Boezio et al., 2000; DuVernois et al., 2001), protons and helium (Bellotti et al., 1999; Boezio et al., 1999), and neutrons (Goldhagen et al., 2004). An overview of historical measurements was compiled by Grieder (2001); in short, many of the past studies focused on primary GCR spectra and their properties but did not systematically investigate the development of the radiation field in the atmosphere. Unfortunately, to date, stratospheric radiation data remain sparse, especially for the case of low or zero geomagnetic shielding parameters; scenarios particularly relevant for the full GCR field in interplanetary space or on planets without magnetic fields. To our knowledge, no dose rate measurements at zero geomagnetic shielding and very low atmospheric shielding levels exist in literature for balloon-flown experiments. Recent radiation measurements at intermediate geomagnetic shielding conditions were made on a balloon flight up to 36 km by the NASA Radiation Dosimety Experiment (RaD-X) campaign (Mertens, 2016; Mertens et al., 2016; Straume et al., 2016; Hands et al., 2016; Norman et al., 2016), with one emphasis of this previous investigation was drawing comparisons with concurrently-flown aircraft at lower altitudes (11 km) (Meier et al., 2016). With such predecessor missions squarely in mind, we aimed to continue expanding knowledge about the radiation conditions in the middle stratosphere by acquiring new measurements on consecutively-flown balloon missions at mid- and polar latitudes. Our first experiment was over New Mexico (resembling the RaD-X campaign flight profile) in September 2019 onboard the NASA Microbes in Atmosphere for Radiation, Survival, and Biological Outcomes Experiment (MARSBOx) payload (Cortesão et al., 2021). This was supplemented by another flight opportunity over Antarctica launched in December 2019 onboard the NASA Exposing Microorganisms in the Stratosphere (E-MIST) payload (Smith et al., 2014), which was carried by the Super Trans-Iron Galactic Element Recorder (Binns et al., 2013; Hams et al., 2016; Rauch et al., 2019) (SuperTIGER)-2.3 mission on a 32-day polar mission that circumnavigated the continent twice. Our measurements captured dose rate profiles in the stratosphere over a wide range of atmospheric shielding (under comparable atmospheric conditions) and for maximum GCR intensity but with different geomagnetic shielding. Taken together, our unique datasets can be compared to model calculations, providing detailed insights into the composition of the middle stratosphere radiation field and the contribution of different particles to the dose rates.

2. Instrumentation and stratospheric balloon flights

This study will provide data to describe the radiation environment measured with the DLR M-42 radiation detector (Berger et al., 2019) onboard two scientific balloon experiments carried out in collaboration with NASA. The high-altitude balloon flights were performed first over New Mexico (MARSBOx experiment) and next over Antarctica (E-MIST experiment). First, we will provide an overview of the radiation detector instrument (section 2.1) followed by

an overview of the space weather conditions (section 2.2). After establishing that background, we provide a description of the MARSBOx and the E-MIST experiments (section 2.3 and 2.4).

2.1 The M-42 instruments for MARSBOx and E-MIST

DLR developed the M-42 radiation detector family (Berger et al., 2019) to have a small, easy-to-use and easy-to-adjust radiation measurement system, adjustable to various payload configurations and robust enough to travel to extreme environments including the upper atmosphere. The M-42 detector is based on one silicon diode with a thickness of 300 µm and an active area of 1.22 cm^2. This configuration enables the measurements of the energy deposition (E_{Dep}) spectra in Si from 0.07 to 20 MeV and the determination of the absorbed dose in Si. Instrument power can come from Li primary or Li-ion rechargeable batteries, or from a micro-USB connector for longer duration flights. For our two balloon missions, version M-42_Compact (M-42_C) of the radiation detector was flown (see Figure 2 in Berger et al., 2019). Hereafter for simplicity, the M-42_C instrument will be denoted as M-42. Table 1 provides the flight details and the dosimeter acquisition specifications. Prior to each balloon flight, the M-42 instruments were integrated into the NASA payload compartments and connected via micro-USB cable to the dedicated power outlets (see further information in section 2.3 for MARSBOx and in section 2.4 for E-MIST).

The measurements were initiated upon balloon launch by providing power to the device approximately 5 min after launch. For the shorter duration MARSBOx mission (~7 hours), a 5 min integration time for the energy deposition spectra was used. In comparison, for the longer duration E-MIST mission (~28 days), radiation data were stored every 30 minutes in the non-volatile flash memory of the instrument. Readout of the M-42 dosimeters was performed upon return to DLR following the balloon missions. Prior to the September 2019 MARSBOx flight, the M-42 was shipped to NASA in July 2019; after the flight the M-42 was returned to DLR in November 2019. For MARSBOx, a total number of 86 data files were stored resulting in 7 hours 10 min of experimental data. Prior to the E-MIST polar flight the M-42 unit was provided to NASA in July 2019; after the E-MIST payload returned from Antarctica, the M-42 was transported back to the DLR in May 2020. For E-MIST, a total number of 1346 data files were stored resulting in 673 hours of experimental data.

Table 1

MARSBOx and E-MIST: space weather conditions and M-42 setup

		MARSBOx	E-MIST
	Location	Ft. Summer, New Mexico	Antarctica
	Date	23 Sept. 2019	15 Dec. 2019 - 21 Jan. 2020
	Sunspot number	1.1±0.3 (Sept. 2019)	1.5±0.5 (Dec. 2019) 6.2±0.7 (Jan. 2020)
	Oulu NM (Cts/min)	6749	6748
	R_C (GV)	3.95	0 - 1.4
M-42	Part Number (P/N)	001	003
	Power	micro-USB	
	Measurement duration	23.09.2019 14:05:33 – 21:15:33	15.12.2019 13:55:35 – 12.01.2020 14:55:35
	Integration intervall (min)	5	30
	Data storage	Non-volatile flash memory	
	Data files (#)	86	1346
	Data duration	7 h 10 min	28 d 1 h

2.2 Space weather conditions during MARSBOx and E-MIST missions

Both balloon flights occurred during the solar minimum between solar cycle 24 and solar cycle 25 under extremely quiet space weather conditions. The monthly mean sunspot number (obtained from http://www.sidc.be/silso/) was very low in September 2019 (1.1±0.3), in December 2019 (1.5±0.5) and in January 2020 (6.2±0.7) (see Table 1). At the time of our measurements, the GCR intensity was near its maximum and comparable to the peak values from the previous solar minimum in 2009 which had reached values unprecedented since the beginning of direct GCR intensity measurements. GCR intensity as measured by Neutron Monitors (NM) was similar during the measurements acquired in New Mexico and Antarctica: e.g. Oulu NM count rate (obtained from https://cosmicrays.oulu.fi/) was 6749 cts/min during the MARSBOx flight (average over 2019-09-23 00:00 UTC to 2019-09-24 00:00 UTC) and 6748 cts/min during the E-MIST campaign (average over 2019-12-15 00:00 UTC to 2020-01-17 00:00 UTC). Also, across our measurements in both locations, variations in the 10 min averages of the NM count rates from the average over the full period were below 2%, showing roughly constant GCR intensities.

Geomagnetic conditions were stable for both balloon flights, as well. The *Kp* index (ftp://ftp.gfz-potsdam.de/pub/home/obs/kp-ap/) reached a maximum value of 1+ during the MARSBOx flight and stayed well below 3 for most of the E-MIST mission with short periods of minor disturbances ($Kp \leq 4$) which did not affect the measurements significantly. The short periods of slightly higher disturbances on 18 December 2019, 6 and 10 January 2020 were caused by faster solar wind streams (bulk speed up to 550 km/s measured by ACE SWEPAM, ftp://ftp.swpc.noaa.gov/pub/lists/ace/) had no distinct effect on GCR intensity. In summary, background GCR intensities during the measurements acquired over New Mexico and Antarctica were effectively identical and the geomagnetic field can be characterized as undisturbed. However, the main difference for the two flight campaigns was the geomagnetic cut-off rigidity (R_C). While this was approximately constant (R_C = 3.95 GV) for the flight over New Mexico, it varied from R_C = 0 GV to 1.4 GV for the Antarctic mission, thereby enabling the comparison of data measured at similar solar conditions but distinct geomagnetic shielding (see further section 3).

2.3 MARSBOx

A complete hardware description of the MARSBOx payload was described elsewhere (Cortesão et al., 2020). The dimensions of the payload were 38.1 cm x 25.4 cm x 63.5 cm with a mass of 18 kg that included a 14.8V, 25.2Ah lithium-ion polymer battery (CU-J141, BatterySpace). The payload was designed to also receive a direct connection to other power sources from a balloon gondola (input range of 9V - 36V) but, due to the short duration of the New Mexico flight, an external battery was used to allow for simpler integration. The M-42 dosimeter was housed in an unpressurized container framed from T-slotted 80/20 aluminum extrusions with white powder-coated aluminum panels to reduce solar heating at float altitudes. Commanding the M-42 and other MARSBOx payload instruments was done through a control panel that had light emitting diodes (LEDs) for indicating system readiness for the onboard computer (OSD3358, Octavo Systems) GPS receiver (GPS_FGPMMOPA6H, Adafruit Industries), camera system (Hero4 Black, GOPRO with Dash controller, CamDo), and heater system. On 23 September 2019 at 14:00 UTC, the MARSBOx payload was launched from Ft. Sumner, New Mexico, USA (latitude: 34.49° longitude: -104.2°) for a mission (LDB #697NT) lasting approximately 7.5 hours; ~4 hours were at the float altitude of ~38 km. The M-42 dosimeter was activated 5

minutes into the launch (at 14:05 UTC) when the balloon was at 3.07 km. At 21:19 UTC on descent at 1.75 km, the M-42 was turned off prior to the gondola with MARSBOx landing at a location northwest of Ft. Sumner (latitude: 35.29° longitude: -105.1°). Figure 1 shows the MARSBOx experiment over New Mexico with a view looking over the horizon. The M-42 was positioned beneath the *red box* indicated in Figure 1.

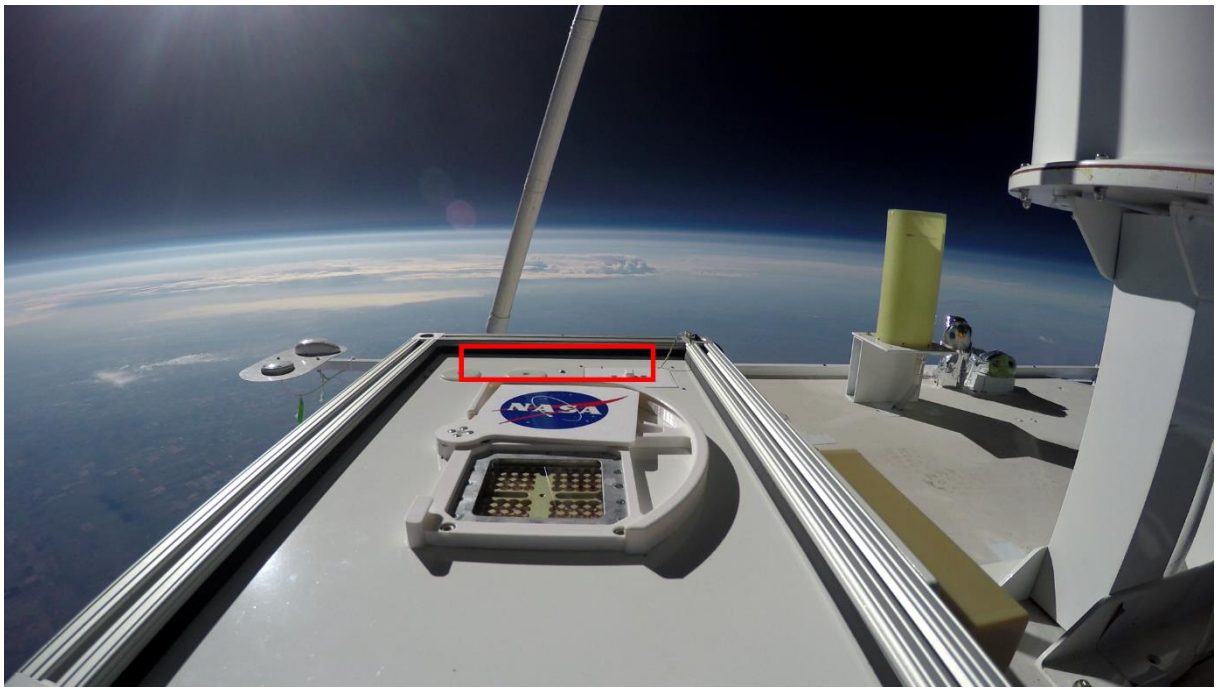

Figure 1. MARSBOx at float altitude (~38 km) over New Mexico, looking out at horizon. The location of M-42 is depicted by superimposed *red box*. © NASA

2.4 E-MIST

Hardware specifications E-MIST payload can be found elsewhere (Smith et al., 2014; Khodadad et al., 2017). After sea vessel transportation to New Zealand in October 2019, the E-MIST payload was flown to McMurdo Station, Antarctica, and mounted onto the sunlit side of the SuperTIGER-2.3 balloon gondola (Rauch et al., 2019) in December 2019 (see Figure A1) at the Long Duration Balloon (LDB) site on ice outside of McMurdo Station for flight LDB #706N. The M-42 dosimeter and other instruments were housed inside the unpressurized E-MIST payload container built from white powder coated aluminum panels and T-slotted 80/20 aluminum framing. System power was provided by a direct connection to the SuperTIGER-2.3 photovoltaic array. During pre-launch time on the Antarctic ice, E-MIST payload components were kept warm by using 8.5 W heating pads (Omegalux Kapton Insulated Flexible Heater, Omega). The payload's avionics system (chipKIT Max32, Digilent) recorded data onto a micro-SD card (BOB-00544, microSD Transflash Breakout, SparkFun), including flight imagery (Hero4 Black, GOPRO with Dash controller, CamDo). Payload commands were derived from an onboard altimeter (MS5607, Parallax). A GPS unit (SPK-GPS-GS4O7A, S.P.K. Electronics Co.) recorded position data throughout the mission.

The 32-day mission was launched on 15 December 2019 at 13:55 UTC and carried into the stratosphere by a 39.5 million-cubic-foot balloon system. Once at float, the balloon altitude

ranged between 33.5 km to 39.3 km, due to periodic thermal conditions. After two full circumnavigations of the continent, each lasting approximately 16 days, the mission concluded and touched down on the ice shelf. The gondola landed about 787 km southeast of McMurdo Station on flat, snow-covered terrain, 2.02 km above sea level (latitude: -71.1255°, longitude: 158.585°) and the E-MIST payload was recovered by a field team on 21 January 2020 (see Figure A2). Figure 2 shows the E-MIST payload over Antarctica with a viewing direction looking downward toward the ice shelf. The M-42 was positioned beneath the *red box* indicated in Figure 2.

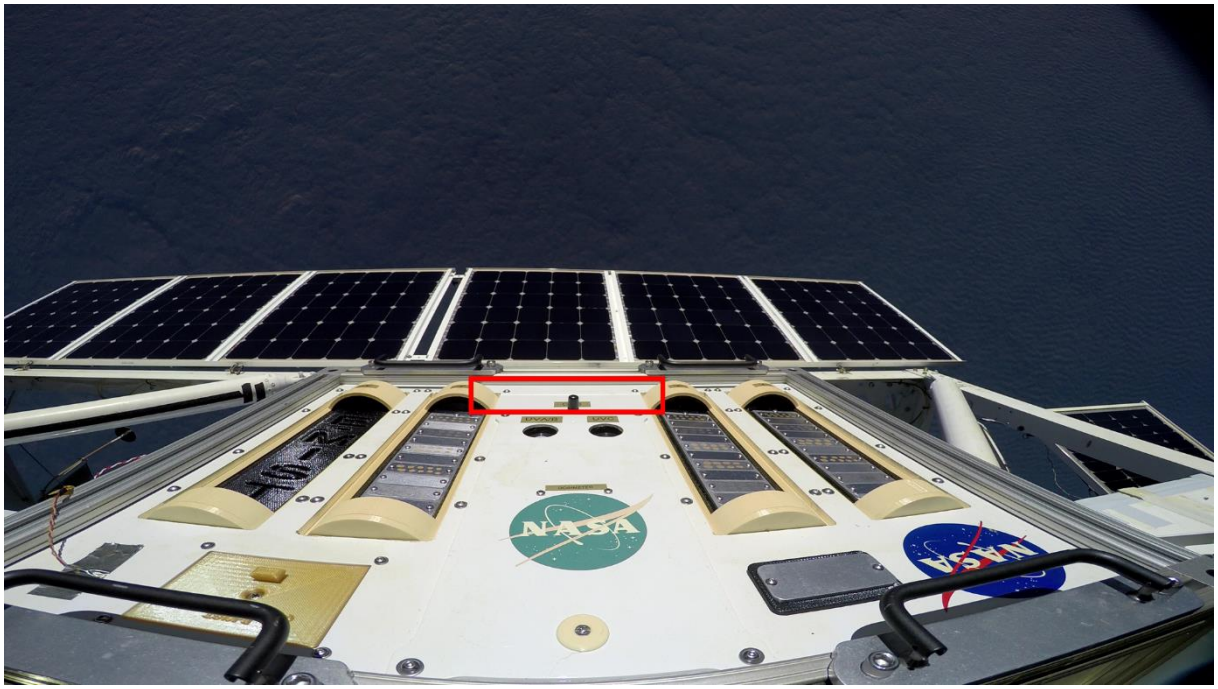

Figure 2. E-MIST at float altitude over Antarctica (~36 km), looking down on the cloud cover below. The location of M-42 is depicted by superimposed *red box*. © NASA

3. Geant4 Simulations

Experimental data taken during the balloon flights were used to validate model calculations of the radiation field in the atmosphere for each location. This approach was particularly important due to the scarcity of dose measurements at altitudes higher than commercial air flights (above about 12 km). The flights were performed at similarly low solar modulation and correspondingly high GCR intensities. Therefore, we could directly compare: (1) model and measurement agreement or disagreement; and (2) dose rate profiles at low geomagnetic shielding in Antarctica and at higher geomagnetic shielding in New Mexico. Furthermore, comprehensive information on composition and energy dependence of the corresponding particle spectra provided by model calculations could be applied towards a better understanding of the radiation field.

In order to perform the model calculations associated to the measurements, the experimental conditions must be reproduced. The most important parameters, apart from altitude, would be geomagnetic shielding quantified by the effective vertical cut-off rigidity R_C and solar modulation. While the latter was almost identical during the two measurement campaigns on

23 September 2019 and between December 2019 and January 2020, R_C differed significantly. While the cut-off rigidity was treated as approximately constant (R_C = 3.95 GV) for the one-day measurement in New Mexico, the variations over the weeks long flight over Antarctica (R_C = 0 GV to 1.4 GV) had to be considered in the model (Table 1).

The cut-off rigidity values for the measurement campaigns were calculated using the PLANETOCOSMICS (http://cosray.unibe.ch/~laurent/planetocosmics/) toolkit for Geant4 (Agostinelli et al., 2003; Allison et al., 2006; Allison et al., 2016) applying the latest version of the International Geomagnetic Reference Field (IGRF-13) (Thébault et al., 2015) for the year 2019 at the corresponding coordinates during the flights and an altitude of 20 km above sea-level. It is noteworthy, that due to the shift and tilt of the dipole-like magnetic field of Earth against the rotational axis, R_C reached during the mission in Antarctica corresponded to geomagnetic shielding conditions at much lower latitudes in Europe (approximately south of Sweden or Scotland) and North America (approximately Montreal or Vancouver).

Primary GCR spectra have been used as described by the model by Matthiä et al. (2013) for primary GCR nuclei from hydrogen to nickel and using the Oulu NM count rates to derive the solar modulation effect and the corresponding model parameter W (W=11.04 for 23 September 2019 and W=11.12 for 15 December 2019 to 16 January 2020). Dose rate profiles were calculated following the identical methodology applied earlier (Matthiä & Berger 2017; Matthiä et al., 2017; Berger et al., 2019), calculating the transport of primary GCR particles through the atmosphere with Geant4 and the resulting particle spectra at a number of different altitudes and corresponding atmospheric shielding. In a second step, the particle spectra at the different altitudes were converted to dose rates through pre-calculated fluence-to-dose conversion factors. For the one-day New Mexico flight conditions, a single set of transport calculations was produced. For the longer duration (32-day) mission in Antarctica two sets of transport calculations were performed for the extreme values of the cut-off rigidity that were reached during the mission (0 GV and 1.4 GV). The dose rates were then calculated by linear interpolation between the values at 0 GV and 1.4 GV at the respective altitudes.

The resulting dose rate was calculated for each particle individually and as a sum, which allowed for tracking the changing contributions through an atmospheric vertical profile. Here, we present the calculated dose rate in Si for different particles and the total dose rate in comparison to the measured dose rate.

4. Results

In the following section 4, we report results from the M-42 detector for the MARSBOx and E-MIST missions. To begin, we present the nominal count rate and dose rate data for MARSBOx (section 4.1) and E-MIST (section 4.2). Next, we compare the MARSBOx and E-MIST data at float altitudes (section 4.3), followed by a comparison of the calculated and measured count- and dose rate data in section 4.4. Finally, in section 4.5, we focus on investigations of the Regener maximum for the two mission profiles. For all absorbed dose data summarized hereafter, we refer to absorbed dose in Si.

4.1 MARSBOx: Measured data

M-42 instrument began logging data for the MARSBOx mission when powered on at 14:05:33 UTC on 23 September 2019 as the balloon started its ascent to the stratosphere. Data were stored every 5 minutes up to the end of the mission (M-42 was switched off at 21:15:33 UTC). Figure 3 depicts flight profile data for the entire MARSBOx mission from

launch to landing. Figure 3a shows the GPS altitude of the mission (km), followed by the temperature (°C) measured with the internal M-42 temperature sensor in Figure 3b. Next, Figure 3c provides the measured count rate (cts/min). The measured dose rate (µGy/h) is displayed in Figure 3e.

In addition, we provide data based on two distinct energy cuts for the energy deposition spectra. The M-42 system measures energy depositions (E_{Dep}) in Si from 0.07 MeV up to 20 MeV. We split this energy deposition range in two intervals, the low energy deposition interval covering all $E_{Dep} \leq 1$MeV and the high energy deposition interval covering all energy depositions $E_{Dep} > 1$ MeV. The relevant percentage for the count rates and dose rates for these two E_{Dep} ranges as denoted before is provided in Figure 3d (count rates) and in Figure 3f (dose rates) of the MARSBOx mission.

The MARSBOx float altitude (~38 km) was reached shortly after 16:30 UTC and the payload remained at this altitude for almost four hours. Shortly after 20:30 UTC, the balloon flight was terminated and the payload on the gondola began its parachute descent with a subsequent touch down at 21:30 UTC. Looking at the count rate data (Figure 3c), we see an increase of counts with increasing altitude, followed by a plateau around 15:00 UTC. From that point forward, the count rate decreased again until about 16:30 UTC (reaching float altitude) and stayed nearly constant to 20:30 UTC upon parachute descent. The relatively rapid descent logged an increase in count rates at around 20:45 UTC followed by a fast drop. We observe these two plateaus in the count rate as related to the crossings of the Regener maximum, i.e., slowly reached during balloon ascent and rapidly flown through during the parachute descent (see section 4.4 and 4.5 for an in-depth discussion).

Examining the percentage of count rates in energy bands compared to mission elapsed time (Figure 3d), we see that the low energy depositions ($E_{Dep} \leq 1$MeV) (starting with 100% close to ground) decreased to 93.5% during the float period (16:30 – 20:30 UTC) with 6.5% being the contributions from high energy depositions $E_{Dep} > 1$MeV. If we compare these values to the percentage contribution to the dose rate (Figure 3 f) for the float time of the balloon, these correspond to 59.2% for $E_{Dep} \leq 1$ MeV and 41.8% for $E_{Dep} > 1$ MeV. In comparison, if we look at the crossings of the Regener maximum during ascent of the balloon, the percentage contribution is 97.3% to 2.8% for the count rate and 78.8% to 21.2% to the dose rate. Altogether, by comparing the Regener maximum conditions with the high-altitude float conditions, we observe an increase in high energy counts (from 2.8% to 6.5%) and the contribution from high energy depositions ($E_{Dep} > 1$MeV) to the dose rate increased from 21.2 to 41.8%. An in-depth discussion with conclusions about these results is provided later in section 4.5.

To summarize, the first maximum in count rates was reached at 14:53 UTC at an altitude of 17.02 km during the ascent of the balloon with a count rate of 107±5 cts/min and a respective dose rate of 3.1±0.4 µGy/h. The second peak was reached at 20:43 UTC at an altitude of 17.02 km during the descent of the payload with an average count rate of 104±5 cts/min and a dose rate of 3.4±0.3 µGy/h. The average dose rate for the float altitude was 2.5±0.4 µGy/h with an average count rate of 54±1 cts/min. Summing up the dose contributions over the whole MARSBOx flight, we arrived at a total mission dose of 16.99 µGy.

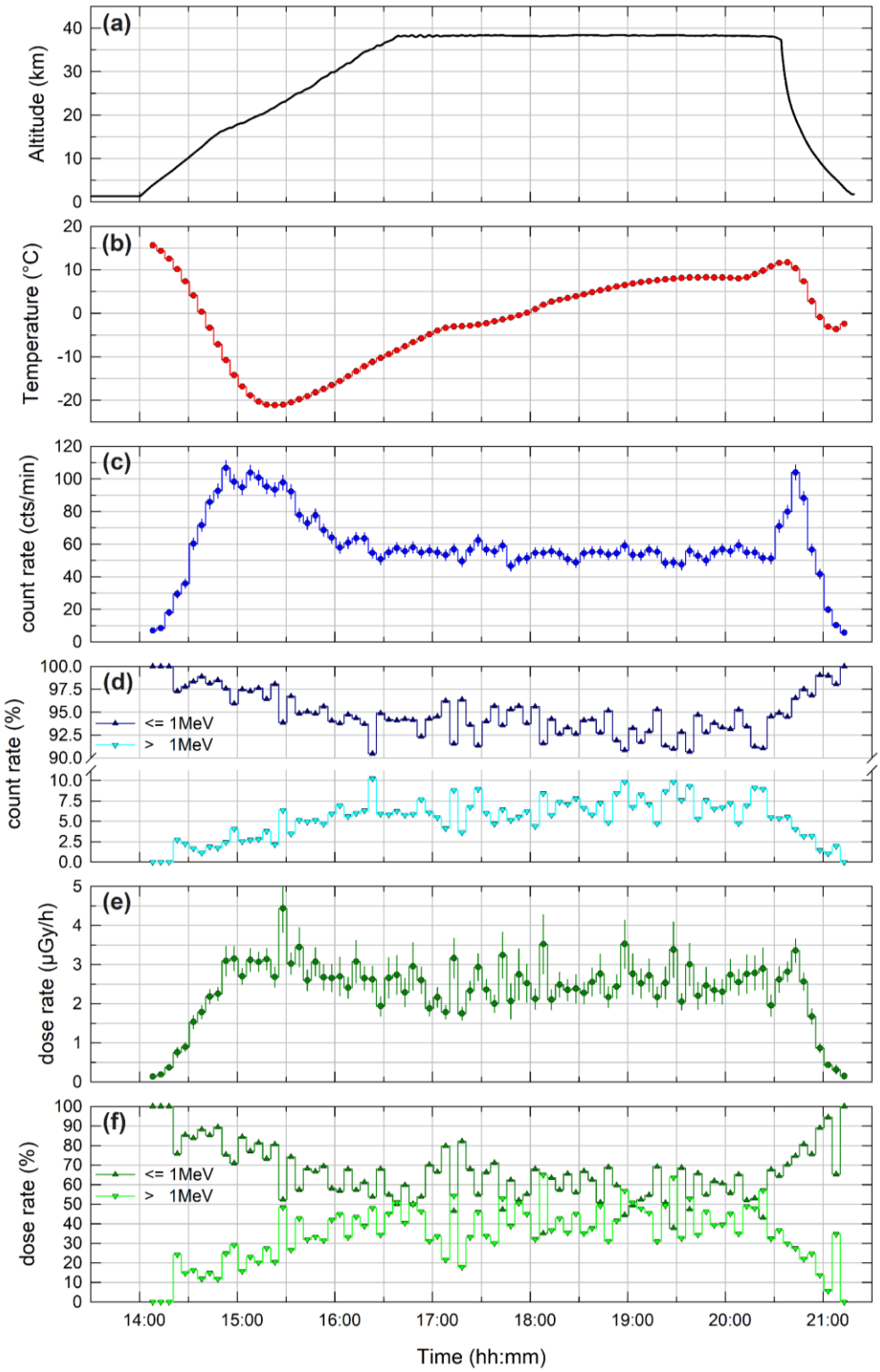

Figure 3. MARSBOx mission data (a) GPS altitude (km); (b) M-42 internal temperature (°C); (c) count rate (cts/min); (d) percentage of count rate for energy depositions $E_{Dep} \leq 1$ MeV and $E_{Dep} > 1$ MeV; (e) dose rate (µGy/h); (f) percentage of dose rate for energy depositions $E_{Dep} \leq 1$MeV and $E_{Dep} > 1$ MeV.

4.2 E-MIST: Measured data

The M-42 detector for the E-MIST mission was powered on 15 December 2019 at 13:55 UTC shortly after the balloon launched from Antarctica. The dosimeter made measurements until 12 January 2020 at 14:55 UTC, covering 28 days and 1 hour of the 32-day mission. In the following section, we present the mission profile data measured by the M-42 system upon E-MIST reaching a float altitude of ~39 km on 15 December 2020 at 19:55 UTC. Data for the first few hours of the mission (during ascent of the balloon) will be reported later in sections 4.4 and 4.5 of this paper.

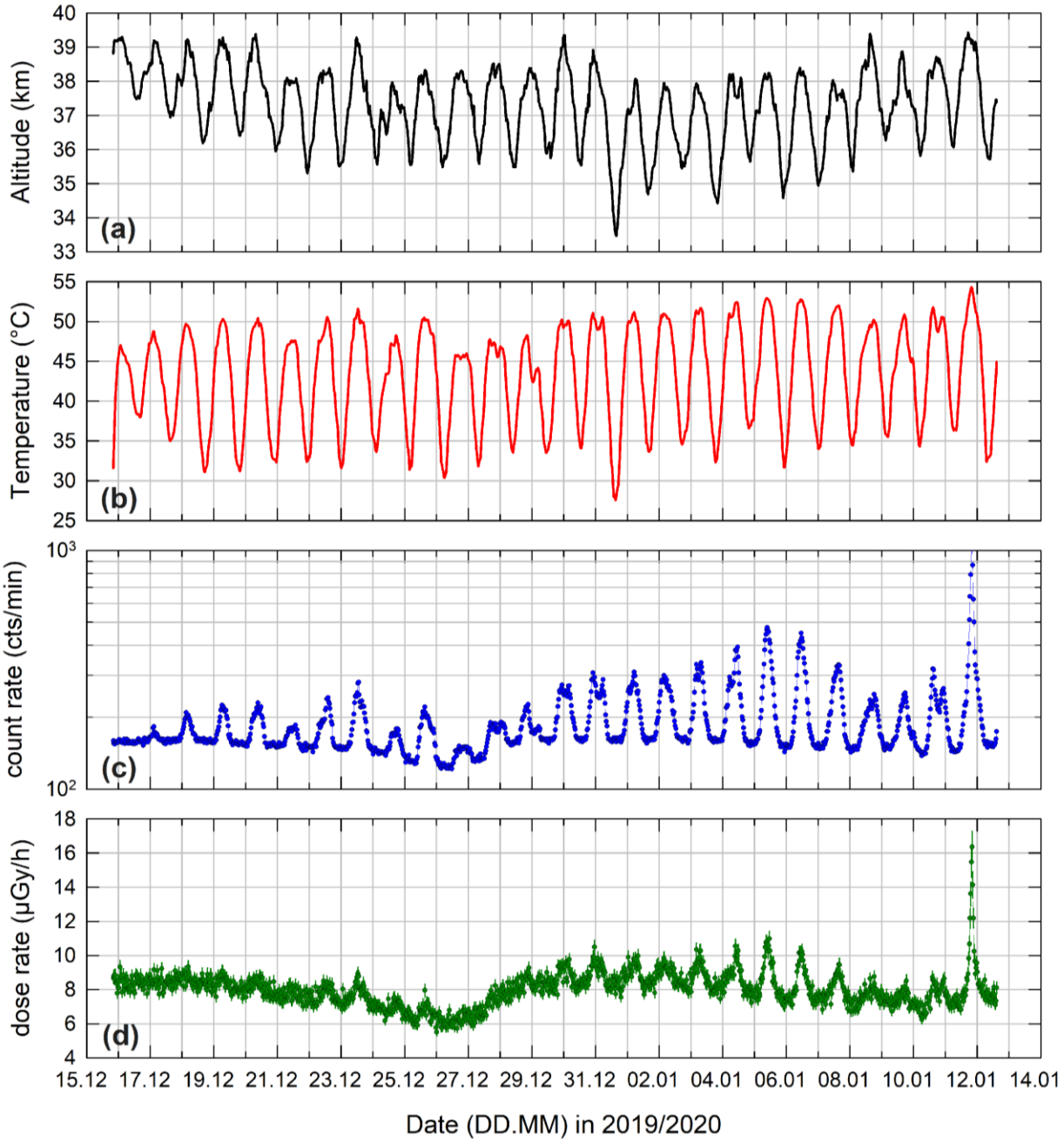

Figure 4. E-MIST mission data (a) GPS altitude (km); (b) M-42 internal temperature (°C); (c) count rate (cts/min); (d) dose rate (µGy/h).

Figure 4a summarizes the altitude track of the E-MIST flight data, which varied about 3 km in periodic cycles due to air temperature influences during stratospheric circumnavigation. The M-42 internal temperature traced the altitude profile pattern depicted in Figure 4b; oscillation values corresponded to the flight altitude (higher altitudes had higher temperatures. M-42 measured count rate (cts/min) are shown in Figure 4c while measured dose rate (µGy/h) is plotted in Figure 4d. The count rate data also showed an oscillation, although less prominent, and lesser still for the measured dose rates. Our initial interpretation of the dataset suggested temperature influenced the M-42 count rate and, to a lesser extent, the dose rate – a topic that will be addressed next.

4.2.1. E-MIST: Measured data (cleaning procedures)

The M-42 radiation detector was designed to work at temperature environments from -20 °C up to ~ +40 °C. Temperatures above ~ 40 °C can lead to unwanted thermal noise in the lowest energy channels of the detector, which then influences both the count- and dose rate measurements of the system. Our internal channel numbering refers to channel #22 as the lowest energy channel used for count rate and dose rate determination with an energy range from 70 – 90 keV. Considering the possible effect of temperature during the E-MIST mission on the lower energy channels of the system (introduced in previous section 4.2), we plotted Figure 5 (a to c) to compare the energy deposition spectra measured by the M-42 system for three different dates (a) 20 December 2019, (b) 05 January 2020 and (c) 10/11 January 2020; each date included two distinct temperature cases: the first case (*cold case*) shows the energy deposition spectra for measured temperature values between 32.7 and 32.9 °C whereas the second case (*hot case*) shows the energy spectra for measured temperature values of 49.8 °C (20 December 2019), 52.6°C (05 January 2020) and 54.3°C (the highest temperature reached during the flight on 11 January 2020).

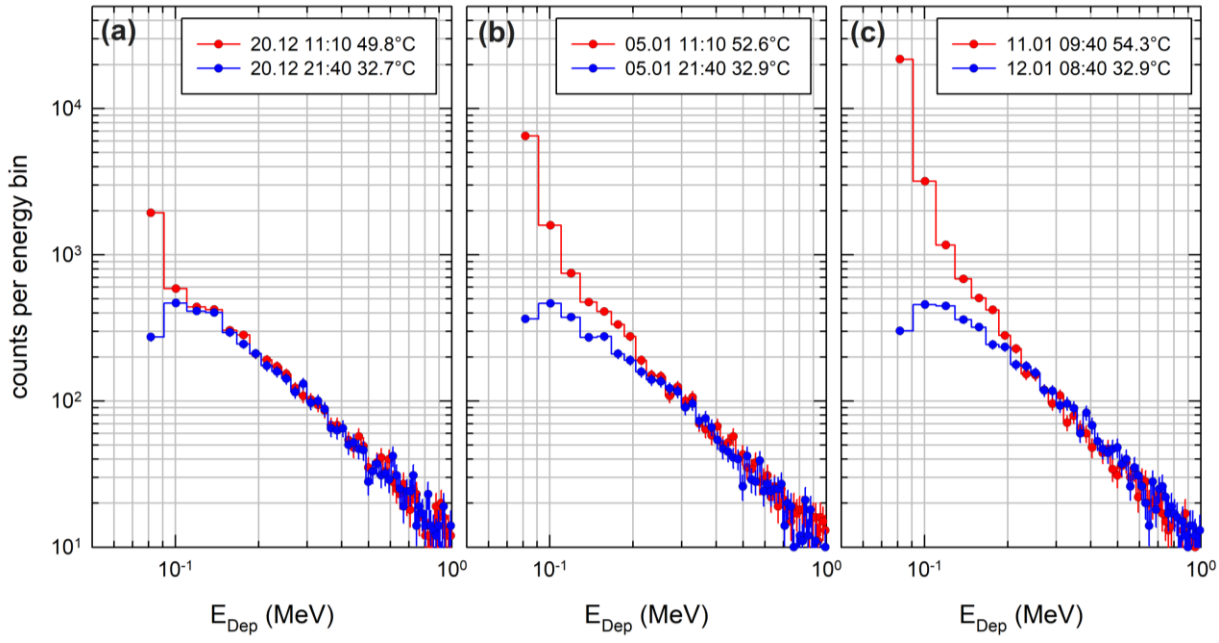

Figure 5. Comparison of *cold* and *hot* energy deposition spectra for three dates within the E-MIST mission: (a) 20 December 2019; (b) 05 January 2020 and (c) 11/12 January 2020. Note: For a better comparison the energy deposition range is limited to $E_{Dep} \leq 1$ MeV.

When comparing the spectra, one clear pattern is the increase of counts in the lower energy bins of the data (up to ~ 180 keV, which equals channel #27 of the spectra) over the duration of the mission (i.e., chronologically depicted across Figure 5a to Figure 5c). From ~180 keV onwards, there was no difference between the two spectra and the relevant dose values for all three comparisons. As example the dose value from channel #27 onwards for the 10/11 January 2020 are 6.43±0.44 µGy for the *hot* case and 6.44±0.46 µGy for the *cold* case. This indicated a need to *"clean"* the data due to effect of increasing temperature on the instrument sensitivity. One straightforward procedure would be to only trust data acquired at temperature values ≤ 40°C, following the M-42 system operating requirements. But such an approach would fail to consider how the oscillation of the count rate increased over the course of the E-MIST mission time (that might be related to an overall temperature creep of the system).

Therefore, a different approach was taken to deal with the thermal uncertainties on system performance, following a two-step progression. The first step limited the data based on the measured count rate in the lowest used M-42 energy channels. If the count rate in channel #22
(70 – 90 keV) was lower than the count rate in channel #23 (90 – 110 keV), the data were considered *clean*. We define *clean* as data not influenced by increasing temperatures. Following this procedure, the total amount of E-MIST mission data on the M-42 was reduced to 262 hours, averaging ~9 hours of data per day. Because the energy depositions and subsequent dose values above ~ 180 keV were not influenced by the temperature, we were aiming to impose a second check on the raw data. The second step had the following logic: If we assume, that from channel #27 onwards, or values of ~ 180 keV (see spectra in Figure 5), there was no temperature influence on the energy deposition spectra, we could use the *clean* data set to generate ratios between count- and dose rates from channel #22 onwards versus count- and dose rates from channel #27 onwards. Then those ratios could be used (based on interpolation) to re-scale the channel #27 count- and dose rate data for the hot temperature cases. This cleaning approach created an additional *interpolated* dataset for the times where the temperature was too high (and M-42 data in the lowest energy channels could not be trusted), and filling in the gaps for a full, cleaned set of mission measurements.

4.2.2. E-MIST: Measured data (*clean + interpolated*)

Based on the information and analysis presented in the previous section 4.2.1., we can now provide the *clean* and the *clean + interpolated* M-42 dataset for the E-MIST mission in Figure 6. We show in Figure 6a the calculated cut-off rigidity (R_C) over the mission. The *clean* dataset is in Figure 6b and Figure 6c. With Figure 6d, we provide the ratio between counts and dose (cts/µGy). The ratio changed over the mission, dependent on R_C. The lower the R_C, the lower the cts/µGy ratio. This indicated that by flying to higher R_C values, the energy deposition spectra changed, and thus, more counts were needed to reach 1 µGy of dose (compared to lower R_C values). Finally, Figure 6e and Figure 6f then show the *clean + interpolated* count- and dose rate profile over the float times for the E-MIST mission. Notably, this dataset represents almost two full circumnavigations of the Antarctic continent by the balloon carrying the payload. The count- and dose rate follow the expected R_C values, reaching the lowest points at 26 December 2019, then climbing again and reaching a second minima on 10 January 2021. The second minimum was not as pronounced, due to the fact that the balloon did not reach the same R_C values as it did for the first minimum (R_C close to 1.4 GV on 26 December 2019; R_C close to 1.0 GV at 11 January 2020).

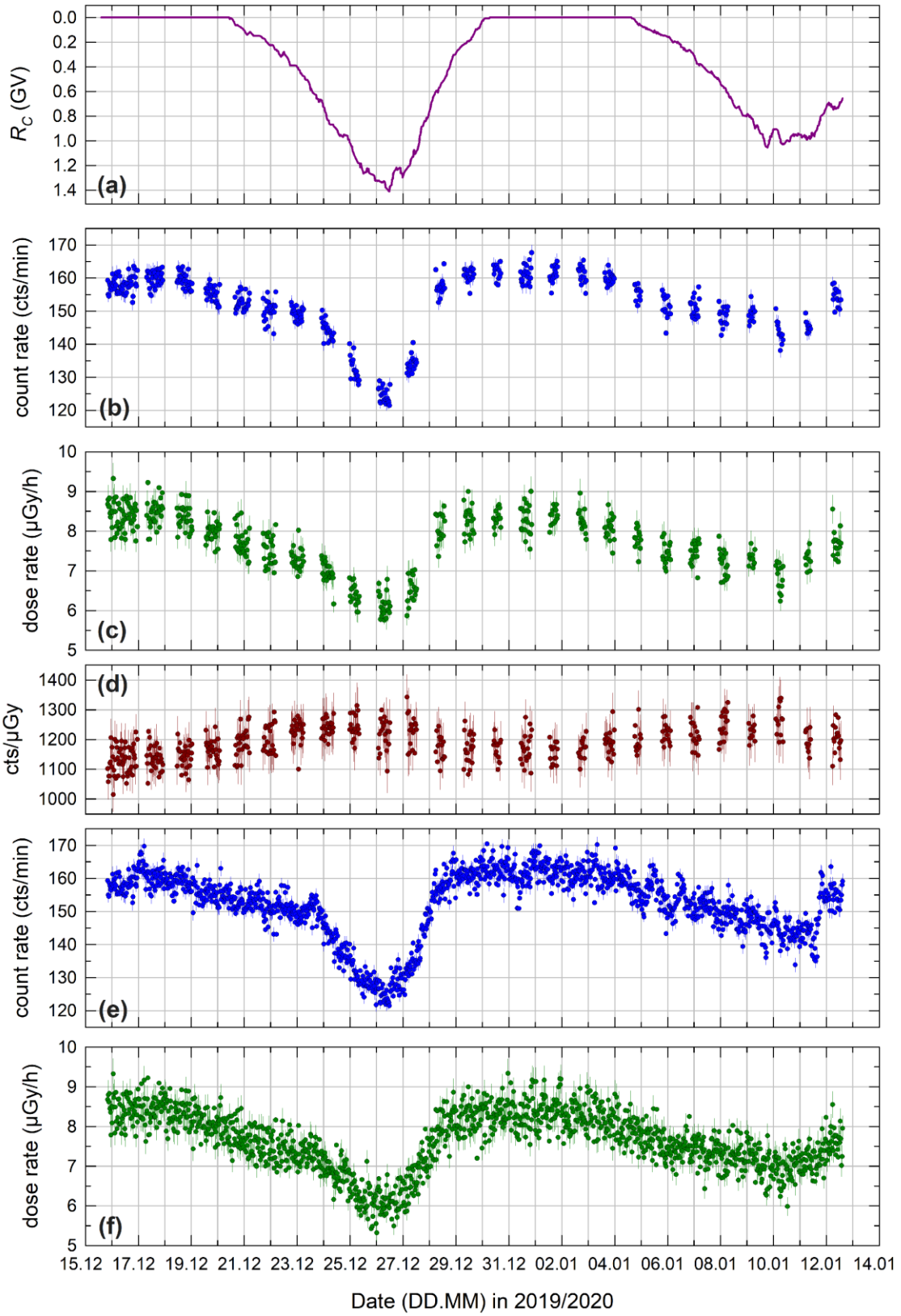

Figure 6. E-MIST mission data (a) cut-off rigidity, or R_C; (b) count rate (*clean*); (c) dose rate (*clean*); (d) cts/µGy; (e) count rate (*clean* + *interpolated*); (f) dose rate (*clean* + *interpolated*)

(see also Figure A4, A5 and A6 for the data of the R_C, the count rate (*clean + interpolated*) and the dose rate (*clean + interpolated*) over the flown mission trajectory).

To better visualize the data, we show in Figure 7a, the average daily R_C and the average daily count- and dose rate values in Figure 7b and Figure 7c, respectively. The count rate pattern mirrored the dose rate pattern, as expected for the related measurements. The total mission dose at float altitude for the 28-day measurement period accounted for 5.1 mGy with a spread in daily dose values of 8.5 µGy/day on 17 December 2019, dropping down to 6.1 µGy/day on 26 December 2019, then reaching maximum values of 8.4 µGy/day on 1 January 2020, before the next minimum of 6.9 µGy/day on 10 January 2020.

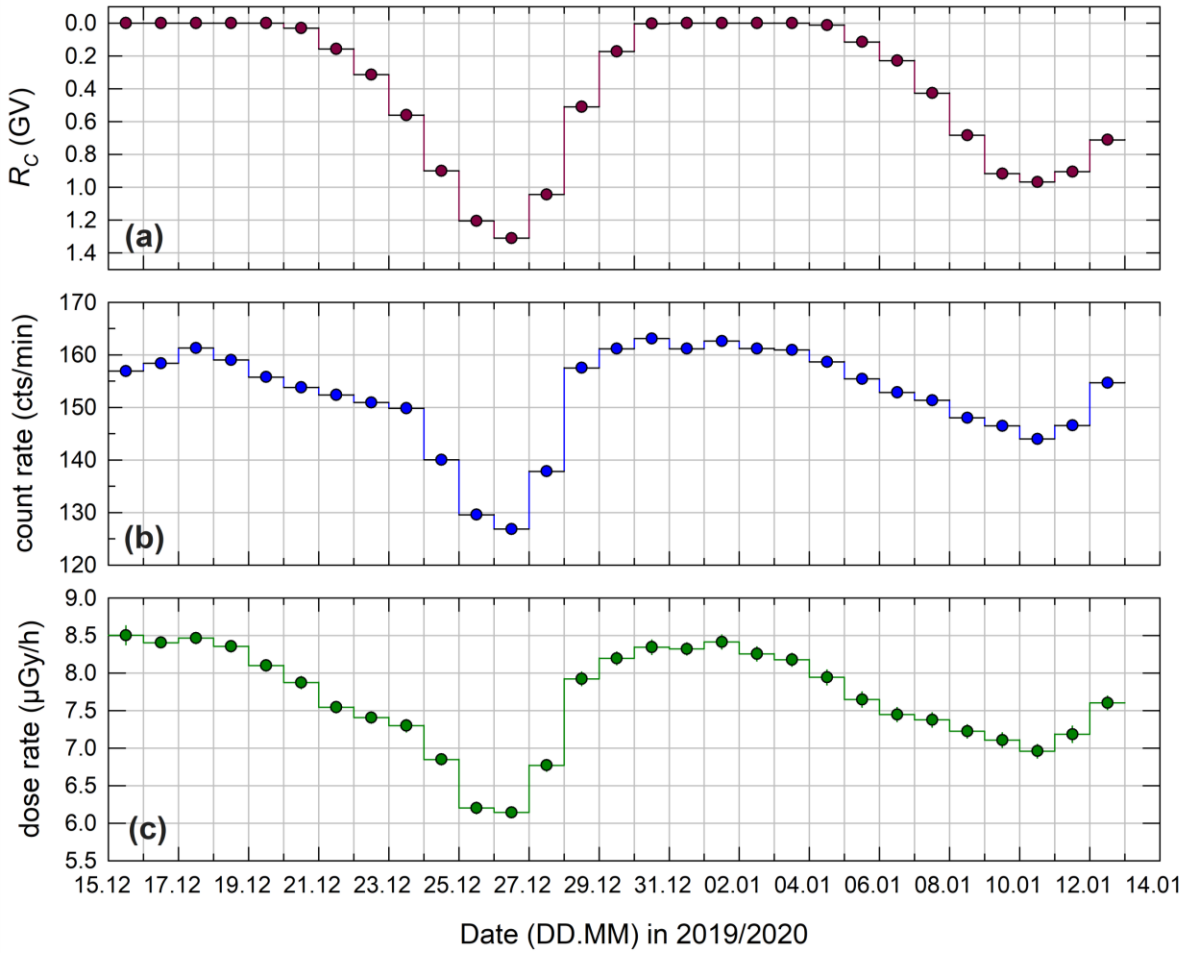

Figure 7. Daily dose values for E-MIST, depicting (a) cut-off rigidity, or R_C; (b) count rate (cts/min); (c) dose rate (µGy/h).

4.3 MARSBOx & E-MIST: Comparison at float altitudes

The following data are based on three hours of measurements for both experiments in order to make direct comparisons of the stratosphere radiation environment for polar and mid-latitude locations. Representative data from MARSBOx over New Mexico were taken for three hours at float altitude on 23 September 2019 from 17:00 – 20:00 UTC. Data from E-MIST over

Antarctica were taken for three hours at float on two different days: 18 December 2019 15:25 – 18:25 UTC and also 26 December 2019 from 03:55 – 06:55 UTC. Two, three-hour E-MIST datasets were chosen based on the fact that on 18 December 2019 the balloon flew at R_C = 0 GV and at 26 December 2019 it reached a R_C of 1.33 GV. All relevant data for this comparison of MARSBOx and E-MIST measurements are summarized in Table 2 and the measured count- and dose rate profiles are shown in Figure 8.

Table 2

Count rates and dose rates for three 3-hour time periods for MARSBOx and E-MIST

Mission	Date	Time	Mean altitude (km)	R_C (GV)	Count rate (cts/min)	Dose rate (µGy/h)	cts/µGy
E-MIST	18. Dec. 2019	15:25 – 18:25	36.3	0	160±2	8.4±0.3	1136
	26. Dec. 2019	03:55 – 06:55	35.7	1.33	125±2	6.0±0.3	1251
MARSBOx	23 Sept. 2019	17:00 – 20:00	38.3	3.95	54±1	2.5±0.4	1256

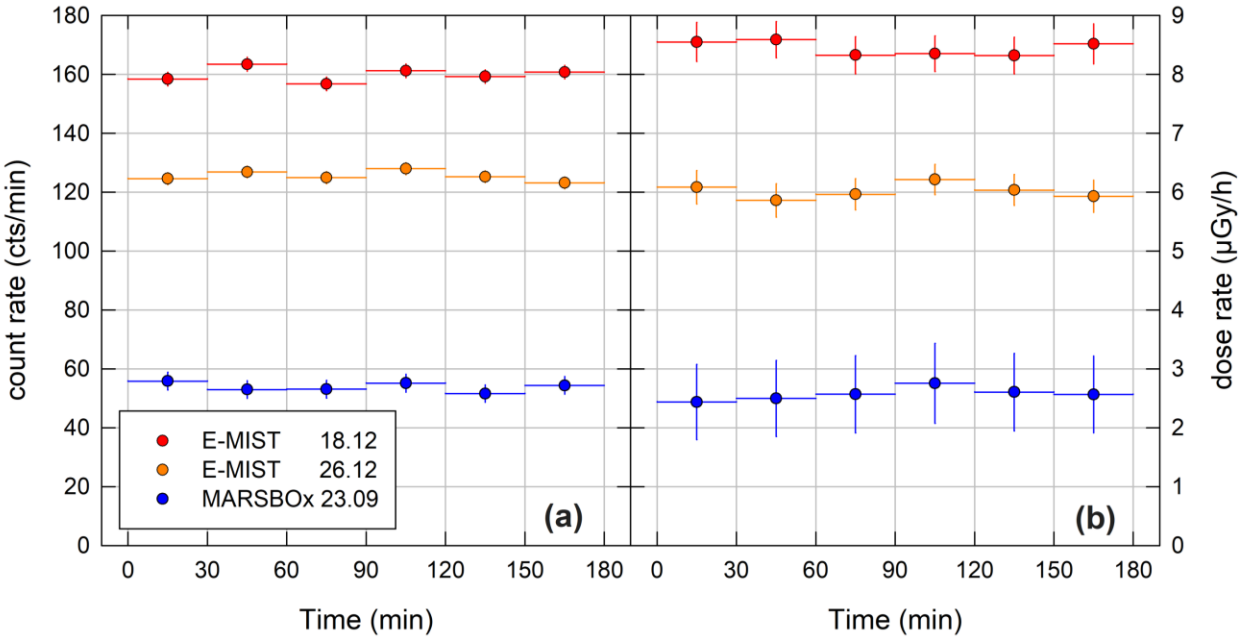

Figure 8. Comparing MARSBOx (23 September 2019) and E-MIST (18 and 26 December 2019) missions over representative, three-hour time intervals with (a) count rate (b) dose rate.

With the E-MIST snapshot, the clear dependence of count- and dose rate on R_C can be noted. The ratio of cts/µGy (i.e., counts needed to reach 1µGy of dose) also increased with R_C, which can be explained by a softening of the energy deposition spectra going to higher cut-off rigidities. Furthermore, by examining the energy deposition spectra for the same 3-hour periods, the effect of the geomagnetic cutoff on the spectra stands out. For instance, in Figure 9a, we depict the spectra for each mission (as summarized in Table 2) with the limitation to E_{Dep} in Si ≤1 MeV. The three spectra clearly differed in dependence on R_C. Next, with Figure 9b, we illustrate the cumulative counts for the three distinct positions over New Mexico and Antarctica – again, this clearly demonstrated the energy deposition spectral reliance on changes in R_C (from

0 GV at 18 December and 1.33 GV at 26 December 2019 for E-MIST and to 3.95 GV for MARSBOx on 23 September 2019).

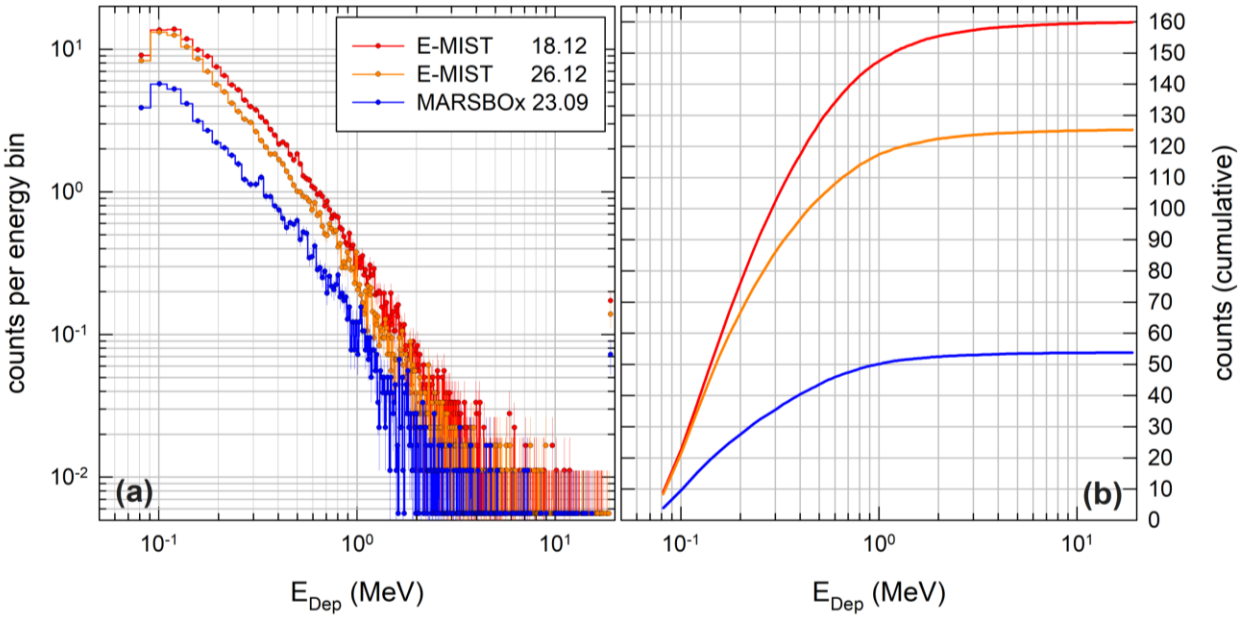

Figure 9. (a) Energy deposition spectra collected over a 3 hr period at float altitude for MARSBOx (23 September 2019, R_C = 3.95 GV) and for E-MIST (18 December 2019, R_C = 0 GV; 26 December 2019, R_C = 1.33 GV); (b) cumulative counts for MARSBOx and E-MIST.

4.4 MARSBOx & E-MIST: Comparing model and measurement results

Within this section 4.4 we will compare model results with the measurements for MARSBOx and E-MIST. First, we will present the calculated dose rate and planar fluence rate for the MARSBOx and E-MIST flights in section 4.4.1. This will be followed by analysis of the correction factors (*cf*) to be applied for the calculated data in order to cope with the energy deposition range (E_{Dep}) of the M-42 system in section 4.4.2. Section 4.4.3 will then present the final comparison of calculated and measured data.

4.4.1. Calculated dose and fluence rates

Geant4 modeling results for dose rate and planar fluence rate of charged particles are shown in Figure 10 and Figure 11, respectively. In each figure, Panel a displays the results for the prevailing conditions during the MARSBOx flight and Panel b for the E-MIST flights. The planar fluence rate represents the number of particles traversing a given plane per area and time, measurable from the recorded count rate of a planar detector divided by its area (e.g., for the M-42 a count rate divided by 1.22 cm^2). For an isotropic field, the particle fluence is two times the planar particle fluence. The solid and dashed lines in the lower panels of Figure 10 and Figure 11 show results for the extreme values of the geomagnetic shielding that were reached during the E-MIST mission (solid lines: R_C = 0 GV; dashed lines: R_C = 1.4 GV). Figure 10 shows the calculated dose rate profile dependent on the atmospheric shielding (altitude) for the different geomagnetic shielding conditions in New Mexico (Figure 10 a) compared to the more extreme values in Antarctica (Figure 10 b).

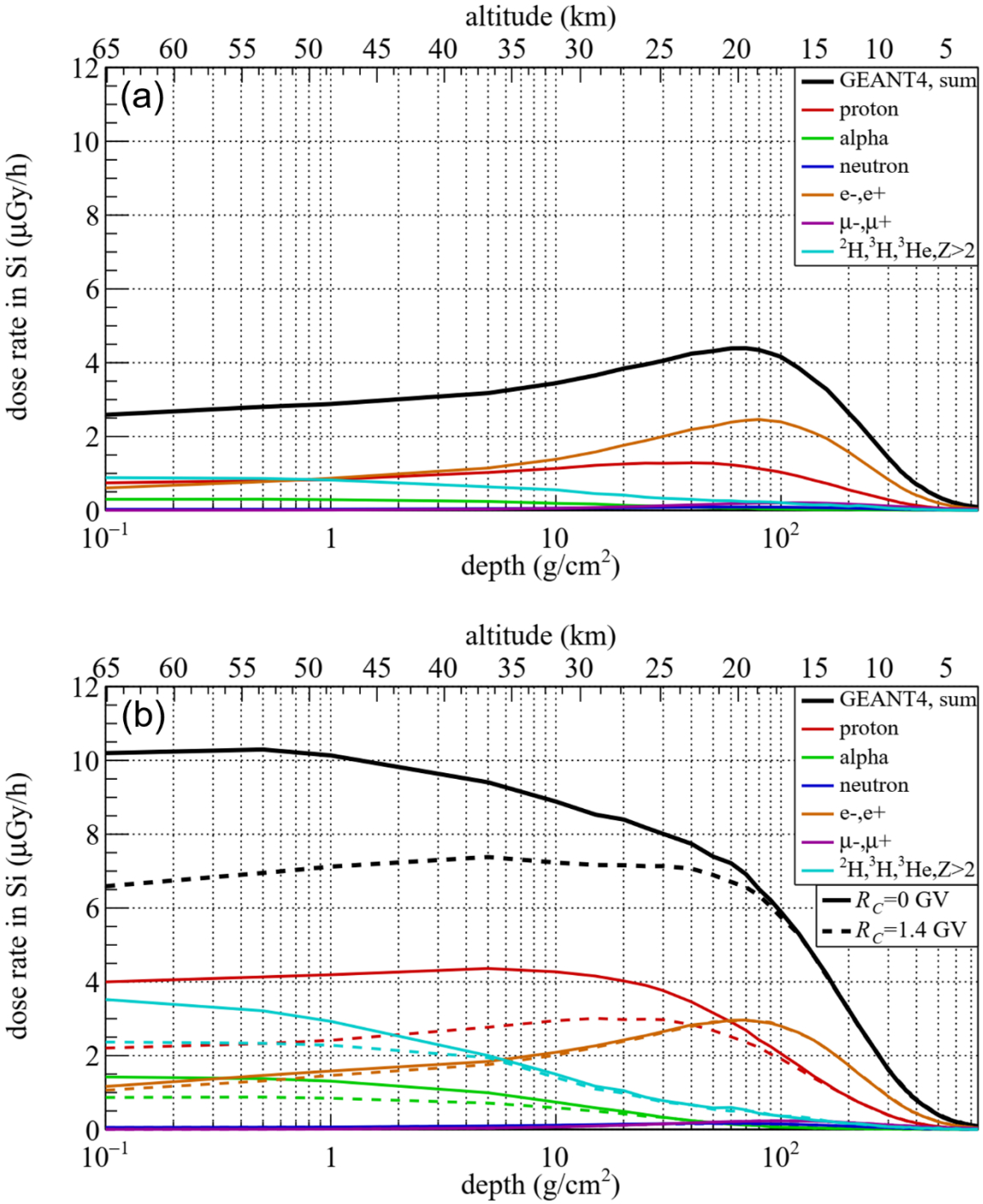

Figure 10. The dose rate in Si as calculated for (a) MARSBOx (R_C = 3.95 GV) over New Mexico and (b) E-MIST (R_C = 0 GV and R_C = 1.4 GV) over Antarctica.

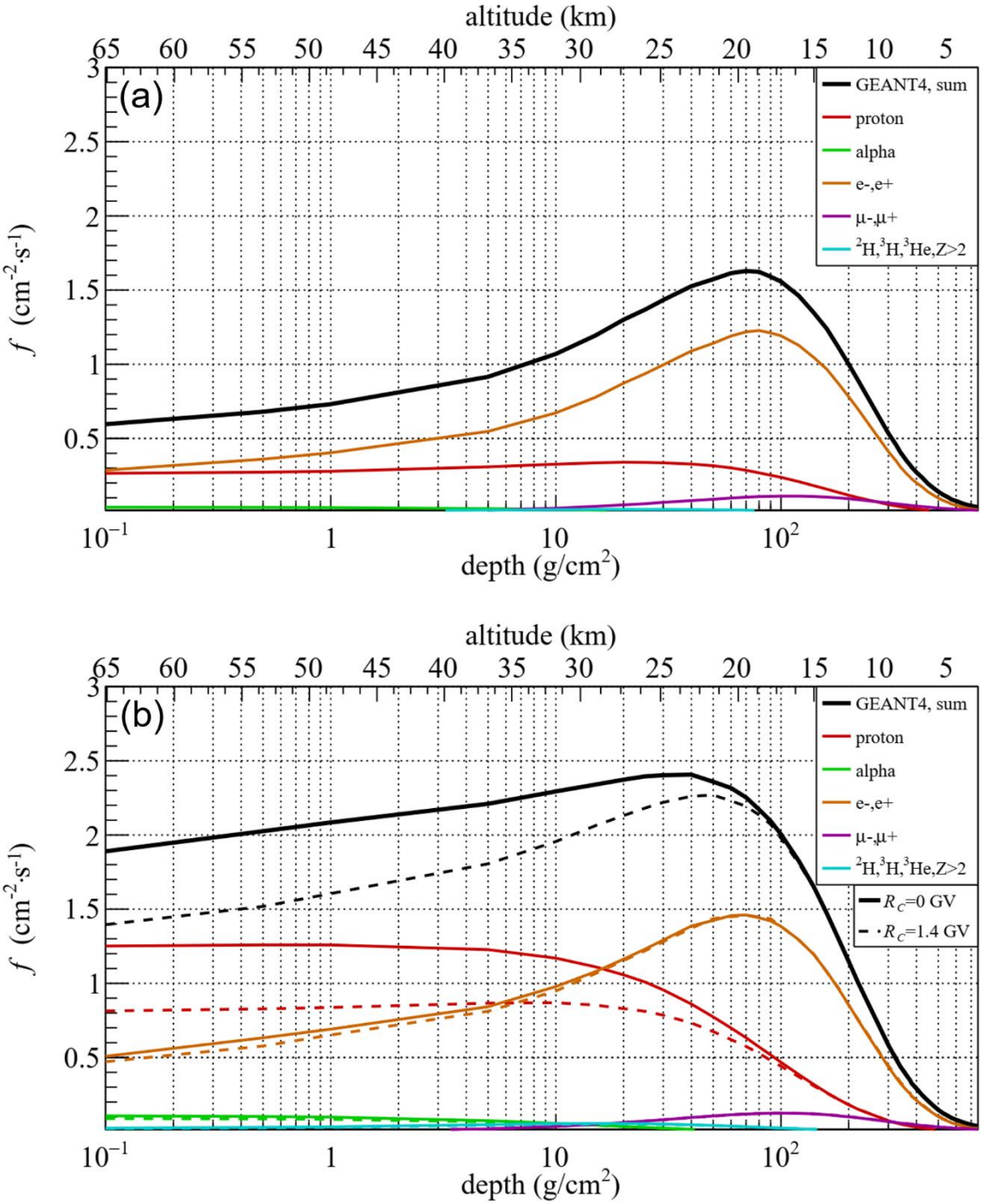

Figure 11. The planar fluence rate of charged particles for (a) MARSBOx (R_C = 3.95 GV) over New Mexico and (b) E-MIST (R_C = 0 GV and R_C = 1.4 GV) over Antarctica.

Our model results predicted dissimilar dose rate profiles for the different conditions: a pronounced maximum in dose rate at around 60 g/cm^2 to 80 g/cm^2 (20 km to 18 km) for the highest geomagnetic shielding at R_C = 3.95 GV in New Mexico, a plateau-like profile reaching approximately constant values above 40 g/cm^2 (≈22 km) for R_C = 1.4 GV, and a dose rate almost

monotonically increasing towards space reaching maximum values at an atmospheric shielding below 1 g/cm^2 (>50 km) for zero geomagnetic shielding over Antarctica. The differing dose rate profiles can be explained by the composition of the radiation field (i.e., the dose rate in Si at higher cut-off rigidities is increasingly dominated by the secondary electron field).

The electron field is much less affected by the geomagnetic shielding and due to the fact, that the electrons are secondary particles created in the atmosphere (electrons contribute only a few percent to the primary cosmic radiation and are neglected in the model), the field has a pronounced maximum between 15 – 20 km (shown in Figure 11). Protons and heavier nuclei, on the other hand, do not show such a clear maximum, neither in dose rate nor in fluence rate. At low geomagnetic shielding, the large relative contribution of protons and heavier nuclei to the dose rate (that additionally increases with altitude), compensated for the decrease in the dose rate from secondary electrons preventing the formation of a maximum (also visible in our Antarctic dataset for E-MIST, see below). For charged particle fluence rate, the situation is slightly different. Although the contribution of protons to the total fluence rate is much greater at low geomagnetic shielding and monotonically increase towards higher altitudes, it cannot quite compensate for the decrease in secondary particle fluence rate. Consequently, and consistent with our experimental data (discussed below), the charged particle fluence rate forms a maximum even at low geomagnetic shielding, but it is less pronounced and at higher altitudes (20 km – 25 km) compared to higher geomagnetic shielding (15 km – 20 km).

4.4.2. Correcting for the sensitivity range of the M-42 detector

When comparing the Geant4 model to the experimental results, the measurement range of the M-42 instrument (0.07 to 20 MeV) must be considered. The limitation to energy depositions above 0.07 MeV and below 20 MeV in the detector meant that a certain fraction of the linear energy transfer (LET) spectrum could not be measured (e.g., for particles perpendicular to the detector the cutoff would be for particles below 0.07 MeV/0.3 mm≈0.23 keV/µm and above 20 MeV/0.3 mm≈66.7 keV/µm). The fraction of dose that was not measured depended on the contribution of low- and high-LET particles below and above the thresholds to the total dose. Using numerical simulations of the distribution of energy depositions in the planar detector, the fraction of dose caused by particles within the sensitivy thresholds of the detector was estimated to be between 0.85 and 0.96 for atmospheric shielding of 5 g/cm^2 (≈36 km), 200 g/cm^2 (≈12 km) and 1000 g/cm^2 (≈0.3 km), as sumarized in Table 3.The fraction was lowest (≈0.87) for high altitudes with an atmospheric shielding of 5 g/cm^2 and it increased toward lower altitudes (≈0.94 at 200 g/cm^2) and grew further near the ground (i.e., during balloon ascent and descent). The lowest shielding approximately corresponded to the maximum altitude that was reached during the ballon flights. The fraction of dose that was measured by the detector also showed a weak R_C dependence and decreased slightly for the geomagnetic shielding corresponding to the mission in New Mexico (R_C≈3.95); an identical trend with higher fractions occurred toward lower altitudes. This trend can be explained by the increasing contribution of high-LET particles, primary GCR nuclei, at high altitudes (thus, low mass shielding), which were above the sensitivity range of the detector. More specifically, an increasing fraction of nuclei undergo fragmentation and would be stopped before reaching lower altitudes, leading to a smaller fraction of high-LET particles. The second trend (also summarized in Table 3) was the increase of the contribution to dose from particles below the sensitvity range of the detector, caused by the formation of the secondary low-LET electron field. This increase, however, was weaker than the decrease in the high-LET particle above the sensitivity range.

Table 3

Calculated fraction of dose for energy depositions E_{Dep} below (E_{Dep} < 0.07 MeV), above (E_{Dep} >20 MeV) and for the sensitivity range (0.07 MeV ≤ E_{Dep} ≤ 20 MeV) covered by the detector. The correction factors cf applied to the modeled dose rates for the direct comparison to the measurements were the factors for energy depositions within the sensitivity range of the detector. The atmospheric depth d is the mass shielding equivalent derived from the pressure in the standard atmosphere at the corresponding altitude. Relevant data is provided for E-MIST at R_C=0 GV and R_C=1.4 GV and for MARSBOx at RC= 3.95 GV.

Mission	E_{Dep} (MeV)	R_C (GV)	d (g/cm^2)	altitude (km)	Dose (% of total)	*cf*
E-MIST	<0.07	0	5	35.91	1.1	
	>20				11.4	
	≥0.07 and ≤20				87.6	0.876
	<0.07	0	200	11.91	4.3	
	>20				1.8	
	≥0.07 and ≤20				93.9	0.939
	<0.07	0	1000	0.275	3.5	
	>20				0.3	
	≥0.07 and ≤20				96.2	0.962
	<0.07	1.4	5	35.91	1.4	
	>20				13.2	
	≥0.07 and ≤20				85.4	0.854
MARSBOx	<0.07	3.95	5	35.91	2.1	
	>20				10.8	
	≥0.07 and ≤20				87.1	0.871
	<0.07	3.95	200	11.91	4.7	
	>20				1.7	
	≥0.07 and ≤20				93.6	0.936
	<0.07	3.95	1000	0.275	3.8	
	>20				0.6	
	≥0.07 and ≤20				95.6	0.956

4.4.3. E-MIST & MARSBOx: calculated and measured data

Planar fluence rates and dose rates versus altitude measured during the ascents of the E-MIST and MARSBOx missions were compared to model data in Figure 12a and Figure 12b, respectively. Measurements are given by solid lines with symbols and model results as dashed lines. Additionally, for the dose rate, the model data were multiplied by the calculated correction factor (*cf*) (dotted lines) for the sensitivity range of the detector (see Table 3) to facilitate a direct comparison to experimental data. In general, the agreement between model and experimental data was strong, with a slight overestimation for the MARSBOx flight, especially for the dose rate at altitudes below 20 km. While the source of this overestimation was unclear, we consider it

a high-priority target for future investigation. Possible explanations include the production of secondary particles that could be overestimated by the model, or that the geomagnetic shielding was not perfectly reproduced by the effective vertical cut-off rigidity that was used in this work.

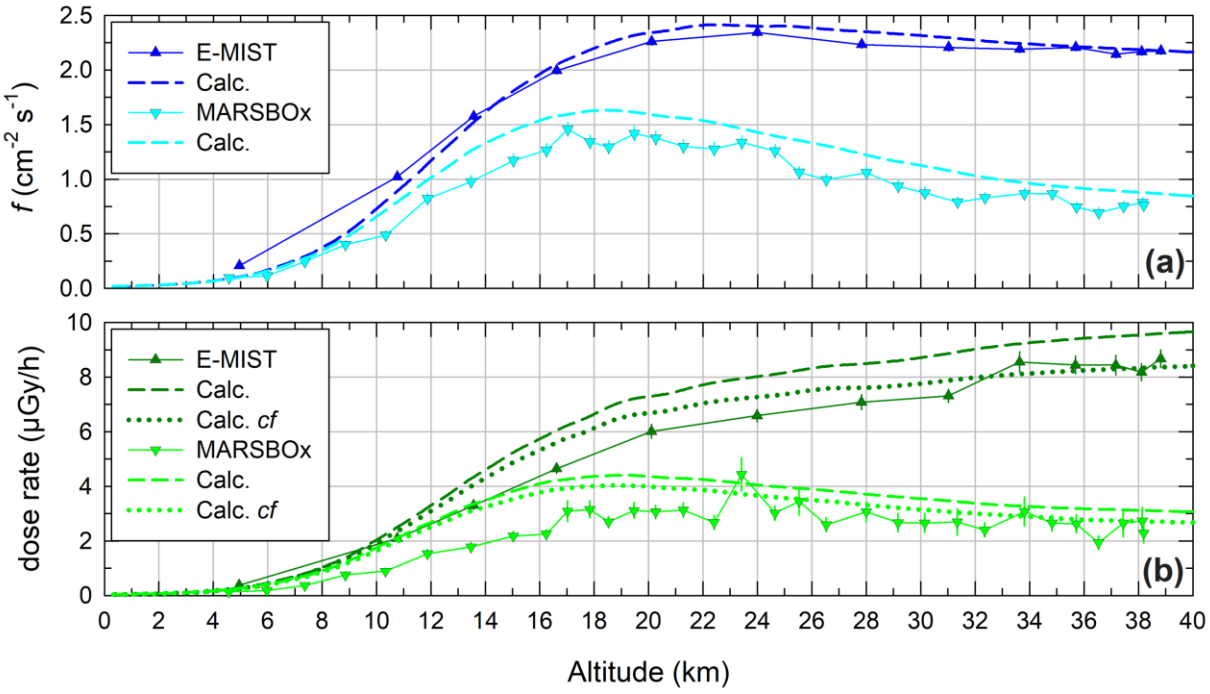

Figure 12. During E-MIST and MARSBOx balloon ascent, comparing measured and calculated (a) planar fluence rates and (b) dose rates. *cf*= correction factor (see text).

One takeway from Figure 12a was confirming the model prediction of a maximum in the fluence rate at around 15 – 20 km at higher geomagnetic shielding (New Mexico, R_C = 3.95 GV) and with less significance the maximum at around 20 – 25 km at low geomagnetic shielding (Antarctica, R_C = 0 GV). Due to the statistical variations in the experimental data, however, it was difficult to identify a maximum in the dose rate (Figure 12b), but it seems plausible. On the other hand, it was clear that no such dose rate maximum exists for low geomagnetic shielding. Also related to this phenomenon is the solar modulation, which likely plays a role in the question if a maximum in dose rate forms in the atmosphere. As introduced earlier, our missions were flown during very weak solar activity and very high GCR intensity. Higher solar activity would suppress the intensity of lower energetic primary particles, leading to the formation of a maximum similar and synergetic to higher geomagnetic shielding. A valuable topic for future research would be to explore the extent to which a stronger solar modulation leads to a clear maximum in dose rate at low geomagnetic shielding, and also how high cut-off rigidities would affect the overall dose rate profile. Herein, our model calculations suggest that for solar maximum conditions, no clear maximum would form in the dose rate profile at zero geomagnetic shielding, but that the curve would flatten and form a plateau similar to the low geomagnetic shielding (Figure 10b, R_C =1.4 GV) and solar minimum conditions.

Another aspect of Figure 12b worth emphasizing is the correction factor (*cf*) for the sensitivity range of the M-42 detector, which can explain most of the discrepancies between the calculated dose rate and measurements (except for the overestimation of the dose rates meaured

during the MARSBOx campaign at altitudes <20 km). Our correction factors were linearly interpolated for altitudes between the values given in Table 3 for each corresponding mission.

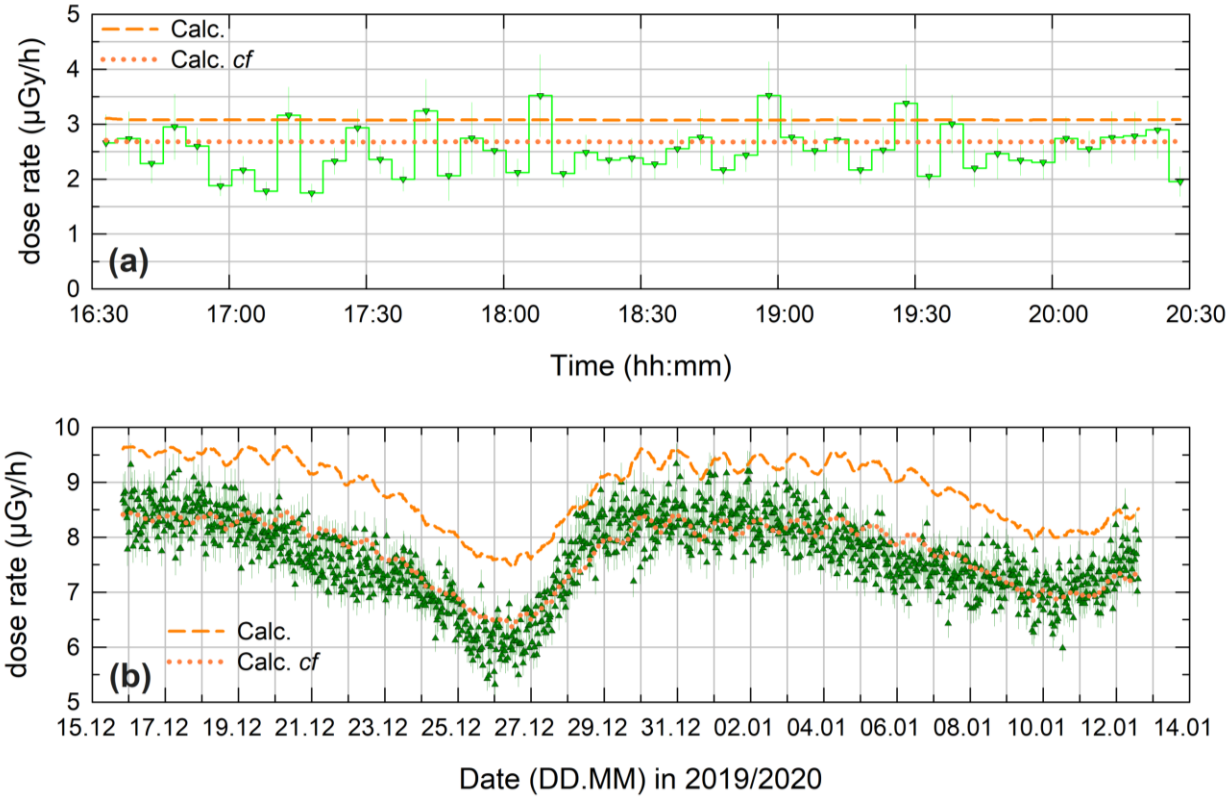

Figure 13. (a) MARSBOx – comparison of measured (green) and calculated (orange dashed lines) and corrected calculated (orange dotted line) dose rate for the time at float altitude; (b) E-MIST – comparison of measured (green) and calculated (orange dashed lines) and corrected calculated (orange dotted line) dose rate for the time at float altitude (see also Figure A7 and A8 for the calculated dose rate (with *cf*) and the calculated dose rate over the mission trajectory).

With Figure 13, we show measured and calculated dose rates at float altitude for the MARSBOx and E-MIST flights over mission time. Our model calculated total dose rates (dashed lines) were multiplied by the M-42 detector sensitivity factor (correction factor *cf*) from Table 3 (dotted line). For the MARSBOx data, a constant factor of 0.871 was applied, corresponding to a cut-off rigidity R_C = 3.95 GV and an altitude of 35.9 km. For the E-MIST data, the corresponding correction factor was calculated from a linear interpolation in the cut-off rigidity along the flight trajectory between the two extreme values at 35.9 km given in Table 3: 0.876 at R_C = 0 GV and 0.854 at R_C = 1.4 GV. From the model, total dose rates for E-MIST were calculated for the boundary conditions of the two, 3-hour intervals in Table 2 and were 9.3 µGy/h (R_C = 0 GV) and 7.6 µGy/h (R_C = 1.33 GV); these values reduced to 8.2 µGy/h and 6.5 µGy/h, respectively, when the corresponding correction factors were applied. The detector sensitivity corrected model values were compatible with the measured data: 8.4±0.3 µGy/h (R_C=0 GV) and 6.0±0.3 µGy/h (R_C = 1.33 GV). The corresponding values for the 3-hour interval from the MARSBOx mission

at R_C = 3.95 GV were 3.1 µGy/h (total calculated), 2.7 µGy/h (calculated times correction factor) and 2.5 ± 0.3 µGy/h (measured).

Interestingly, Figure 13 also demonstrated how the overestimation of the model data could be consistently explained by the limited measurement range of the detector. For instance, variations of the dose rates caused by changing geomagnetic shielding along the E-MIST flight path were nicely reproduced by the model when applying the effective vertical cut-off rigidity to the primary GCR spectra. In addition, measurements performed by the DLR Eu:CROPIS RAMIS (Hauslage et al., 2018) detector (at approximately 600 km altitude in a polar orbit at the time of the E-MIST flight) also indicated that the additional dose in Si from energy depositions between 20 MeV and 200 MeV accounted for ~12% of the total dose in the south polar region.

4.5 MARSBOx & E-MIST: The Regener Maximum

After summarizing measured and modeled radiation results, we now transition to data analysis for crossings of the Regener maxima during each balloon flight mission, starting with MARSBOx (section 4.5.1) and followed by E-MIST (section 4.5.2).

4.5.1. MARSBOx – ascent and descent

The count- and dose rate data provided in Figure 3 show two crossings of the Regener maximum; one during the slow ascent of the balloon system over New Mexico and the other during the fast descent of the payload (on parachute after mission termination the descent rate was ~1.4 km/min).

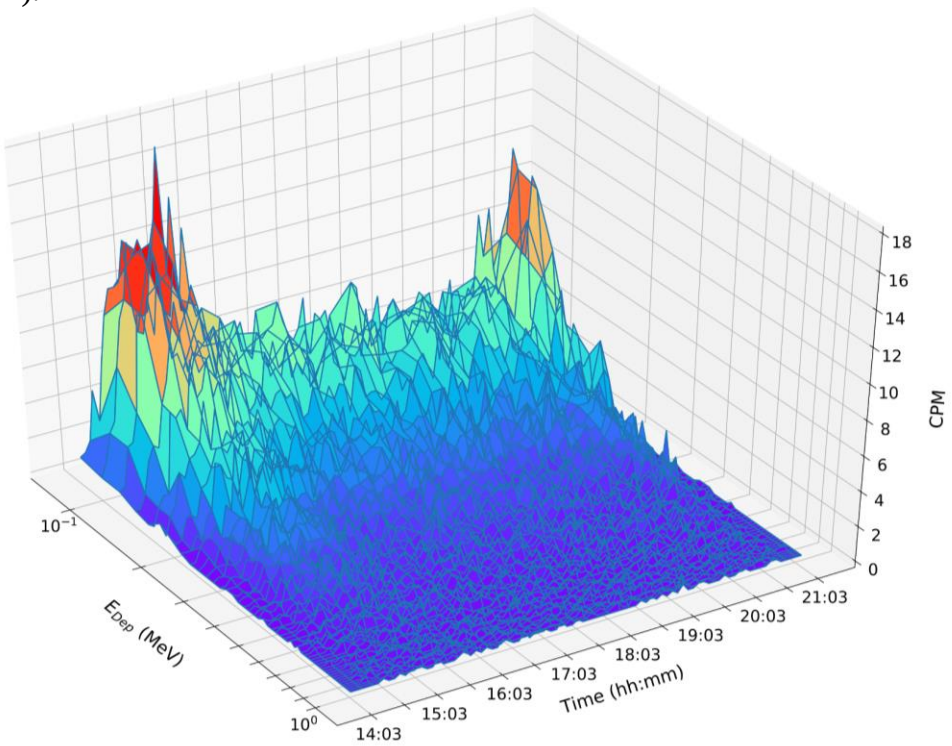

Figure 14. MARSBOx energy deposition spectra over the full New Mexico mission (for energy depositions $E_{Dep} \leq$ MeV in Si).

To further illustrate and investigate the Regener maxima, Figure 14 presents the energy deposition spectra (limited to $E_{Dep} \leq 1$ MeV) across the full MARSBOx mission. Two clear

peaks at the start (14:53 – 15:13 UTC) and at the end (20:43 UTC) of the mission were noteworthy. The peaks appear only in the lowest energy deposition channels for MARSBOx up to ~400 keV, indicating that the dominant source in the low energy regimes was electrons (see also calculations for the count rate in Figure 11 a).

First, we will focus on comparing the count- and dose rate profiles for the slow ascent and the fast descent of MARSBOx, partitioned as total energy deposition spectra plus the relevant cuts for low energies (E_{Dep} ≤1MeV) and high energies (E_{Dep} >1MeV).

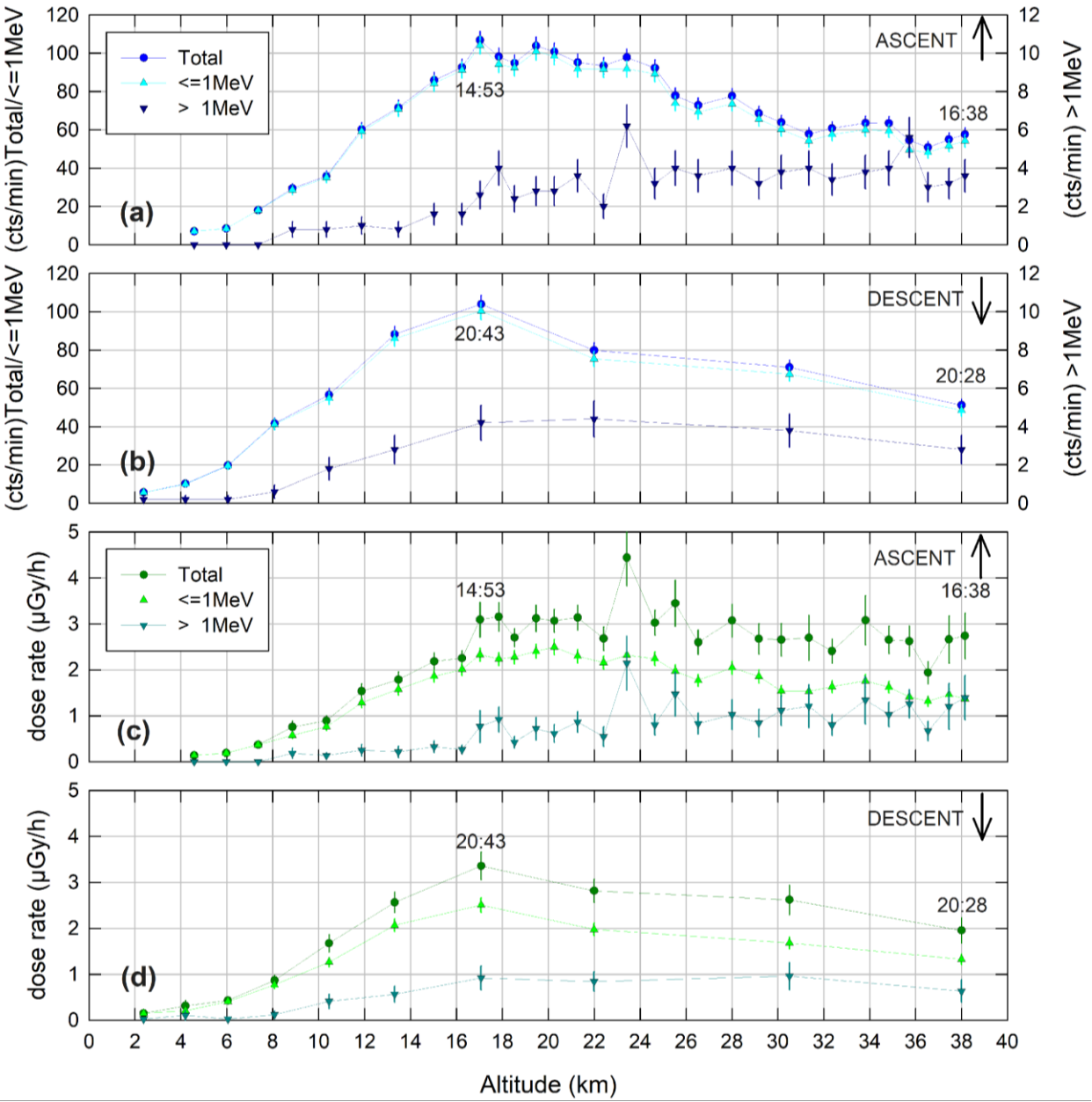

Figure 15. Count- and dose rate versus altitude for MARSBOx over New Mexico: (a) total count rate and count rate for energy regimes E_{Dep} ≤ 1 MeV and E_{Dep} > 1 MeV for the ascent of the balloon (b) same data for the descent; (c) total dose rate and dose rate for energy regimes E_{Dep} ≤ 1 MeV and E_{Dep} > 1 MeV for the ascent of the balloon (b) same data for the descent.

The relevant ascent data are provided in Figure 15a and Figure 15c, showing the count- and dose rates up to float altitude at around 16:30 UTC. The descent data are displayed in Figure 15b and Figure 15d, again with count- and dose rate values for the payload starting ~38 km altitude at 20:28 UTC.

During ascent, the first maximum in count rates was reached at 14:53 UTC at an altitude of 17.02 km. This maximum was also seen in the dose rates, at least up to 15:13 UTC, where the maxima remained both in count- and dose rates, and then slowly declined until a stable float altitude. Averaging across five data points (from 14:53 – 15:13 UTC) with altitudes ranging from 17.02 to 20.26 km yielded a count rate of 101±2 cts/min and dose rate of 3.0±0.4 µGy/h.

During the descent of the balloon carrying MARSBOx, the M-42 instrument reached its maximum of count- and dose rates at 20:43 UTC, with a count rate of 107±5 cts/min and a respective dose rate of 3.3±0.4 µGy/h. In comparison to ascent and descent data, the average dose rate for the mission's float altitude was 2.5±0.4 µGy/h with an average count rate of 54±1 cts/min (see also Table 2).

Based on results for the fluence rate presented earlier in Figure 11a, and to generate a comparison of the possible changes in the energy deposition spectra over the mission phases, we can go even further by looking at three distinct flight locations (ascent, float, descent), as summarized in Figure 16. With Figure 16a, the averaged spectra for ascent (from 14:53 – 15:13 UTC), float (from 17:00 – 20:00 UTC) and descent (20:43 UTC) were depicted. Next, Figure 16b compares the cumulative count rate for ascent, float and descent.

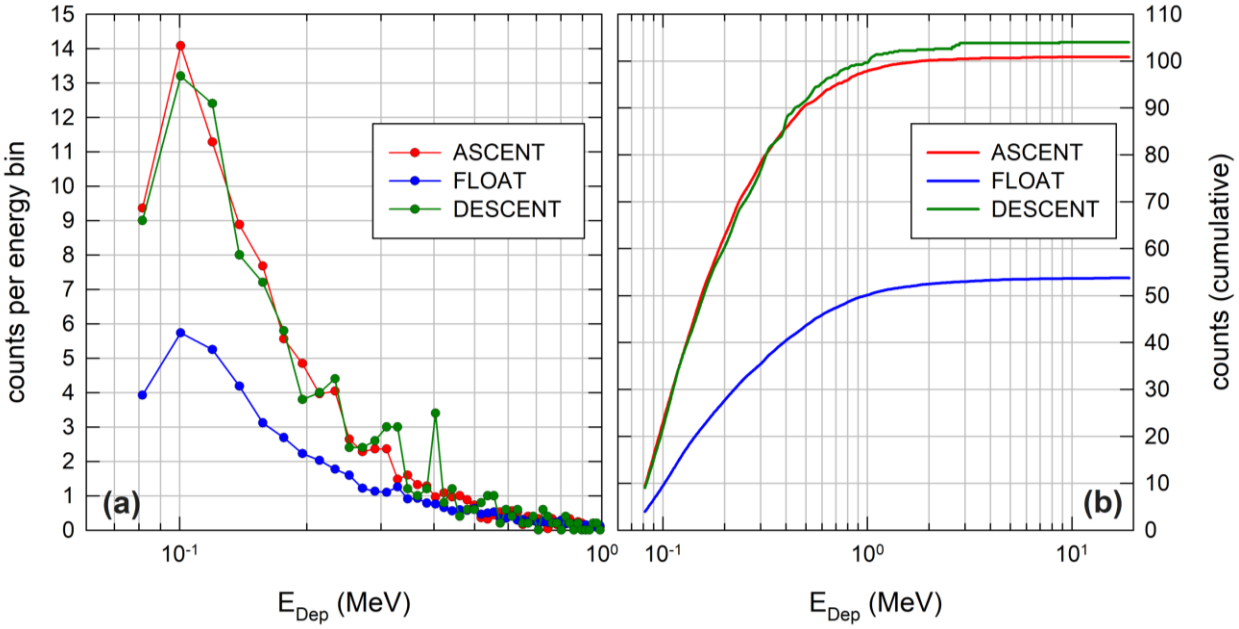

Figure 16. (a) MARSBOx energy deposition spectra (limited to $E_{Dep} \leq 1$ MeV) for the ascent, float and descent of the mission; (b) cumulative counts for ascent, float and descent.

The peak in energy depositions at ~100 keV for both ascent and descent profiles in Figure 16a was striking in comparison to the data at float altitudes and can be related to the peak in electrons at this altitude (see Figure 11a). Even though we only have one data point (20:43 UTC) for the descent of the balloon, the values seemed to mirror the ascent, thereby showing where the Regener Maximum crossing occurred. By focusing on the cumulative counts, overlap

between ascent and descent can be noted, with a clear distinction compared to the float altitude. For instance, the counts beneath and above 1 MeV were nearly the same for ascent and descent (97% ≤ 1MeV and 3% >1MeV), but changed to 93% ≤ 1MeV and 7% > 1MeV at float altitudes. Together, this showed the difference between energy deposition spectra during the MARSBOx mission and the clear distinction, which can be made to quantify the Regener maximum, standing out from results measured at float altitude.

4.5.2. E-MIST - ascent

In this section, we analyze the conditions during E-MIST ascent. Pertinent count- and dose rate data from launch upon reaching the ~39 km float altitude is provided in Figure 17. Data acquisition started at 13:55 UTC with the middle of a 30-minute integration interval for the M-42 detector at 14:10 UTC. From there (14:10 up to 20:10 UTC), the count rate profile increased, reaching a maximum at 16:40 UTC (172±2 cts/min), and, finally, started a decrease with values at 20:10 UTC of 159±2 cts/min. Unlike the count rate, the dose rate slowly increased over the entire duration of the ascent. These result will be explored in Figure 18 and the discussion below.

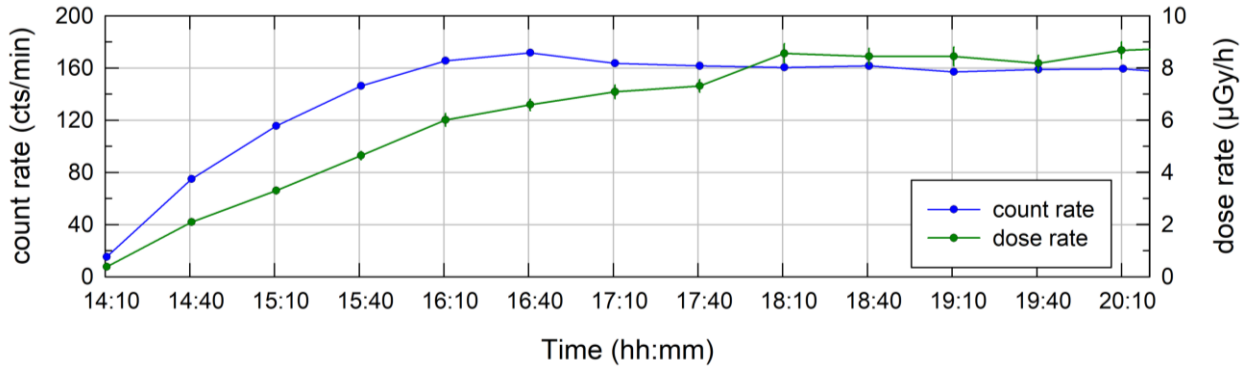

Figure 17. E-MIST over Antarctica during the 6-hour ascent of the balloon: count rate (cts/min); dose rate (µGy/h).

Figure 18a and Figure 18b reveal the dependence on altitude for the total energy deposition spectra and at regimes E_{Dep} ≤ and E_{Dep} > 1 MeV, for count- and dose rate, respectively. Looking at 4 specific times from 15:40 to 17:10 UTC, can help illustrate the pattern. The maximum in total count rate occurred at 16:40 UTC, also observed for the low energy cut; while the count rate for the high energy cut > 1 MeV increased steadily upon reaching the final float altitude. Meanwhile, for the dose rate profiles (Figure 18b), values increased upon reaching float altitude, while the dose rate for ≤ 1 MeV already reached a plateau at 24 km (16:40 UTC). The dose rate profile for the energy regime > 1MeV flattened out around 34 km (18:10 UTC). Table 4 compiles count- and dose rate data for the aforementioned time periods.

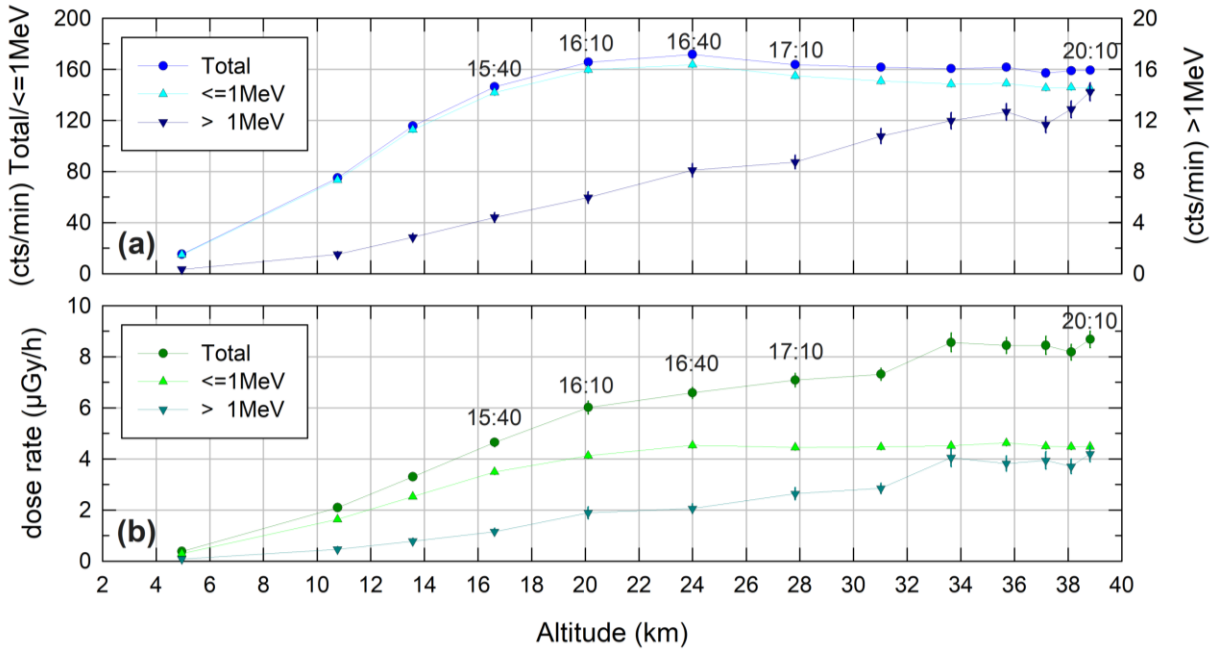

Figure 18. E-MIST: (a) total count rate and count rate for energy regimes $E_{Dep} \leq$ and $E_{Dep} > 1$ MeV for the ascent of the balloon; (b) total dose rate and dose rate for energy regimes $E_{Dep} \leq$ and $E_{Dep} > 1$ MeV for the ascent of the balloon.

Table 4

Count rate and dose rate data for the Regener maximum plus data for float altitude for E-MIST

		Time (hh:mm) (UTC)				
		15:40	16:10	16:40	17:10	20:10 (float)
Altitude	km	16.62	20.11	23.99	27.82	38.82
Altitude range		14.99 – 18.13	18.13 – 21.89	21.89 – 26.10	26.10 – 29.61	38.46 – 39.11
Count rate	Total	146±2	166±2	172±2	164±2	159±2
	≤1MeV	142±2	160±2	164±2	155±2	145±2
	>1MeV	4±0.40	6±0.45	8±0.52	9±0.55	14±0.70
Count rate (%)	≤1MeV	97.0	96.4	95.3	94.7	91.1
	>1MeV	3.0	3.6	4.7	5.3	8.9
Dose rate	Total	4.6±0.2	6.0±0.3	6.6±0.2	7.1±0.3	8.7±0.3
	≤1MeV	3.5±0.1	4.1±0.1	4.5±0.1	4.4±0.1	4.5±0.1
	>1MeV	1.2±0.1	1.9±0.2	2.1±0.2	2.6±0.2	4.2±0.3
Dose rate (%)	≤1MeV	75.1	68.6	68.8	62.8	51.7
	>1MeV	24.9	31.4	31.2	37.2	48.3

The count- and dose rate data from when the payload reached float at 20:10 UTC are of special significance and were also included in Table 4 for comparison. At 16:40 UTC, around

95% of the count rate was for energy depositions ≤ 1 MeV. This value decreased to 91% at float altitude, indicating that the spectra itself changed, hardening for the higher altitudes. A similar behavior was observed for the dose percentage. At 16:40 UTC, only 31% of the dose was from energy depositions > 1MeV, and the value rose to 48 % at float altitude, again indicating harder spectral conditions. We also noticed the pattern for MARSBOx mission values, where at float it was a 42% dose contribution from high energy depositions. Taken together, and when applied to E-MIST over Antarctica, we can conclude the balloon reached its Regener maximum in count rates at 16:40 UTC with an altitude of ~24 km (the exact altitude range over the 30-minute integration period was 21.89 – 26.10 km). But we must also consider the different parts of the energy deposition spectra to determine if E-MIST crossed the maximum at this point during the mission, and not rely solely upon the total count rate for this interval (with the detector measuring energy depositions up to 20 MeV in Si). So, in Figure 19 we provide a three-dimensional energy deposition spectrum limited to $E_{Dep} \leq$ 1MeV for the first 15 hours of the mission (similar to Figure 14 for MARSBOx). With this approach, the peak of counts in the lowest energy regime, shortly after the start of the mission, was readily identifiable. Moreover, the lower energy deposition regime (up to 200 keV in Si) flattened out and then stayed relatively constant at float altitudes and onward during the mission.

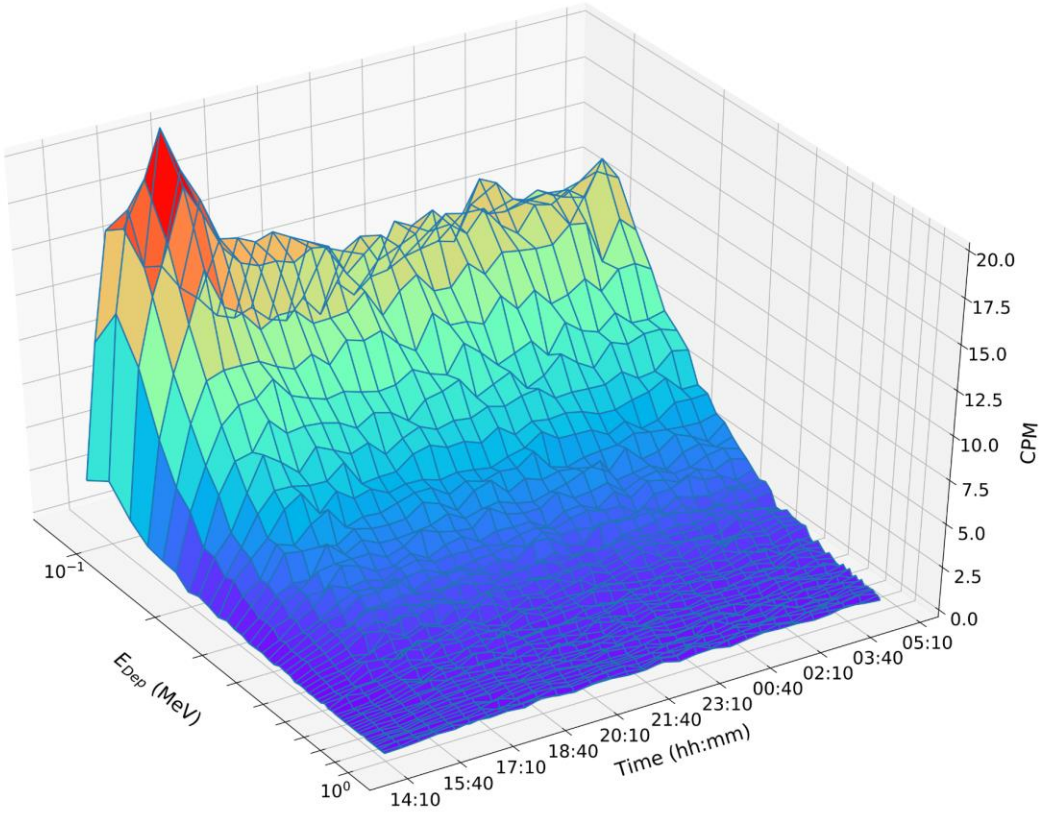

Figure 19. E-MIST energy deposition spectra for first 15 hours of the Antarctic flight during balloon ascent (for energy depositions $E_{Dep} \leq$ MeV in Si).

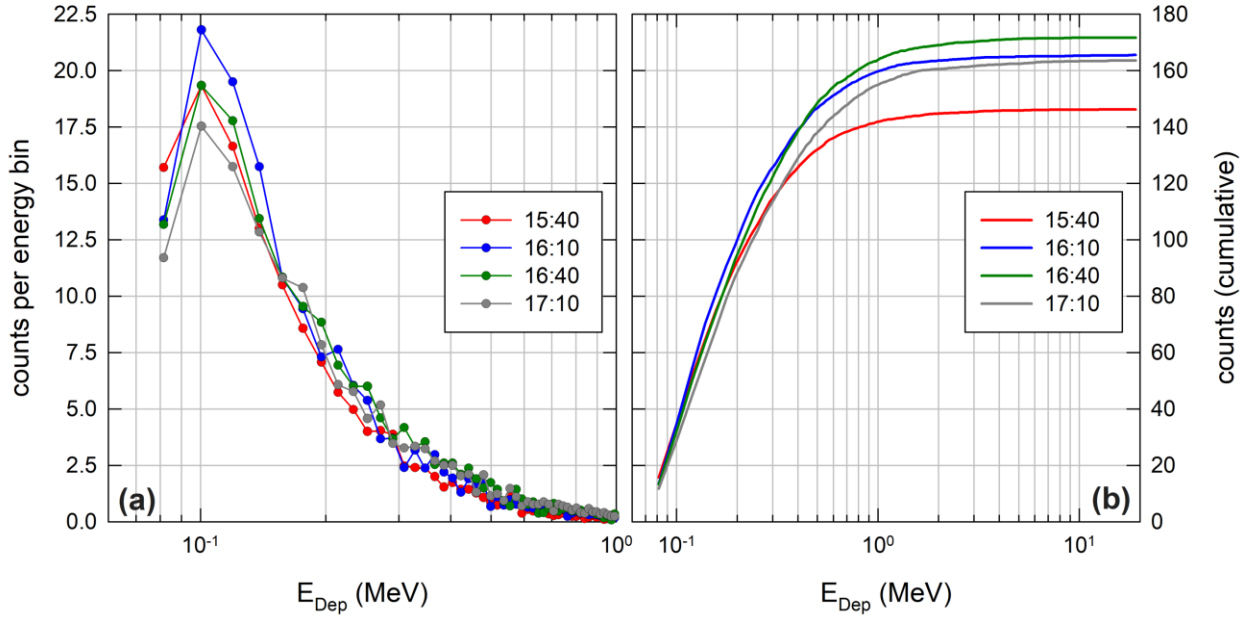

Figure 20. (a) Energy distribution and cumulative counts for 4 distinct time periods of E-MIST float (limited $E_{Dep} \leq$ MeV in Si); (b) cumulative counts.

After applying this refined focus, we now see a peak closer to 16:10 UTC with the balloon altitude of 20.11 km (altitude range 18.13 – 21.89 km); rather different from the earlier identified peak at 16:40 UTC when only the total count rates were considered. To further investigate this peak, we examined the energy deposition spectra for the four periods of interest (15:40 – 17:10 UTC) in Figure 20a, with Figure 20b showing the cumulative count integrated over the whole energy range of the spectra. Yet again as with Figure 16 for MARSBOx, Figure 20 showing the peak at 16:10 UTC consistent with the 3D spectra (Figure 19), and we observe the peak of electrons in the relevant altitude range as flown through at 16:10 UTC consistent with the calculated count rate profile (Figure 11b).

Considering this pattern we can conclude another maximum of count rates was reached (in the lowest energy channels) at 16:10 UTC due to the electron contributions during ascent of the balloon, even though the maximum of the total count rate was reached at 16:40 UTC for the whole energy range of the M-42 instrument. Our assertion is supported by Figure 20b, where the cumulative count rates at 16:10 UTC were at maximum, but only up to ~ 400 keV. From this energy deposition point onward to 16:40 UTC the instrument yielded maximum count rates of 172±2 cts/min.

5. Summary and Conclusion

With two consecutively-flown, high altitude balloon mission observations within a four-month timeframe (23 September 2019 to 12 January 2020) from New Mexico and Antarctica, we demonstrated it is realistic to obtain robust radiation environmental data by using a small, simple-to-integrate radiation detector system (M-42). Our results provide, for the first time, a direct comparison of mid-latitude and polar stratosphere radiation conditions in a region of the

Earth's atmosphere that remained largely uncharacterized to date. The similarities and differences in GCR at these disparate locations set the stage for refining future measurements while validating Geant4 model predictions. We observed a cut-off rigidity for MARSBOx over New Mexico of around 3.95 GV, whereas E-MIST over Antarctica results ranged from 0 GV up to 1.4 GV during the stratospheric circumnavigation of the continent. Our data showed a clear dependency of count- and dose rates based on: (a) the site of the flights; (b) the cut-off rigidity comparing the two flights; and (c) the changes in cut-off rigidity for conditions over Antarctica. With the mid-latitude, relatively short-lasting New Mexico flight, average dose values were 2.5±0.4 µGy/h. In sharp contrast, Antarctic average dose values were much higher, reaching 8.4±0.3 µG/h at 0 GV cut-off rigidity. With the New Mexico mission, our count rate and the dose rate datasets displayed a crossing of the Regener Maximum during both ascent and descent between 17.5 and 20 km. By comparison, the Antarctic datasets included a Regener maximum only in count rates at an altitude of 24 km, but not in the measured dose rate. The values for measured data remained within the error bars of our Geant4 simulation, with the strongest alignment during Antarctic float altitudes and deviations that could be corrected by adjusting to known limits of the energy deposition regime for the M-42 detector. The maximum measured daily dose values over Antarctica reached 202 µGy/day (at R_C =0 GV), a level of particular significance for the space exploration community, considering we have observed similar dose values (212 µGy/day) on the surface of Mars across equivalent time periods, as measured by the Curiosity rover (Berger et al., 2020). Short of sending experiments or instruments to the Red Planet, or as a progressive stepping stone for eventually journeying into deep space, our dosimetry results support the idea that long duration Antarctic balloon missions can be used for accurately introducing experiments or instruments to sustained Mars-like radiation conditions.

Appendix A: E-MIST

Within this appendix we provide additional figures for the E-MIST mission.

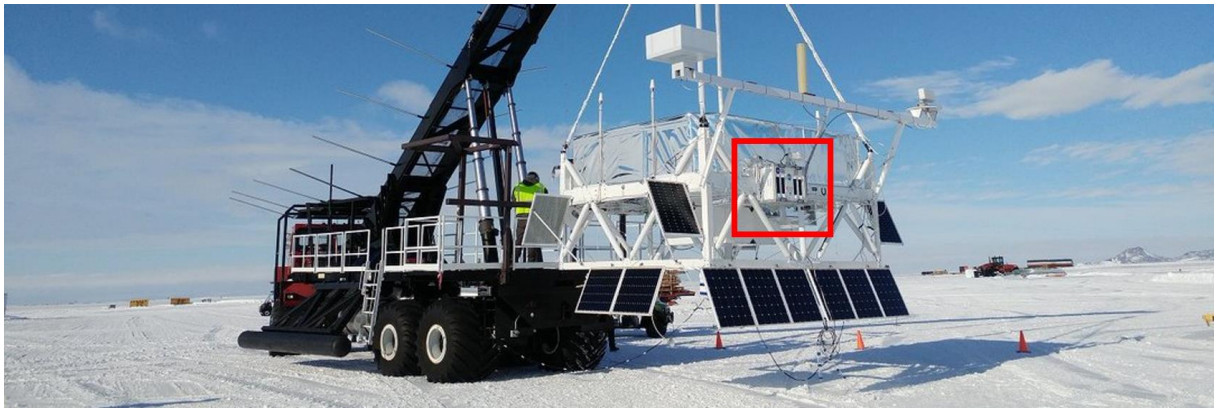

Figure A1. The SuperTIGER-2.3 balloon mission payload carrying E-MIST and the M-42 detector, shortly before launch from Antarctica on 15 December 2019 (*red box* around E-MIST payload with the M-42 detector) © NASA

Figure A2. The SuperTIGER-2.3 balloon mission (*red box* around the E-MIST payload with the M-42 detector). Picture was taken during the payload recovery operation after landing on the Antarctic ice shelf, following the 32-day mission in the polar stratosphere. © NASA

In the following section, we provide additional graphical representations of the data for the E-MIST mission as 2D plots following the mission trajectory of the E-MIST mission.

Figure A3 shows the 2D plot for the timeline of the mission.

Figure A4 shows the 2D plot for the calculated cut-off rigidity (R_C).

Figure A5 shows the 2D plot for the measured count rates (*clean + interpolated*).

Figure A6 shows the 2D plot for the measured dose rates (*clean + interpolated*).

Figure A7 shows the 2D plot for the calculated dose rates applying the correction factor (*cf*).

Figure A8 shows the 2D plot for the calculated dose rates.

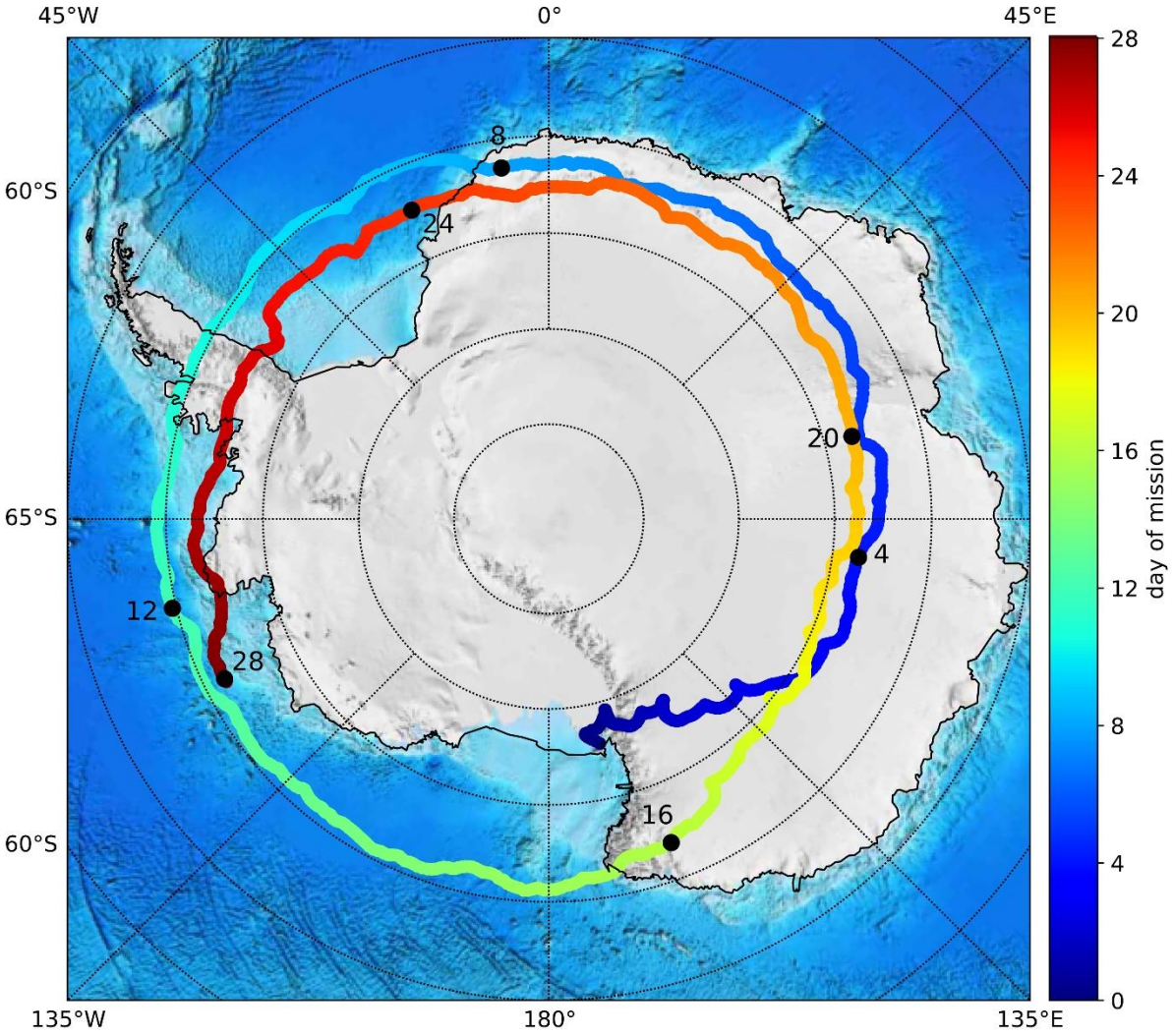

Figure A3. The E-MIST flight profile.

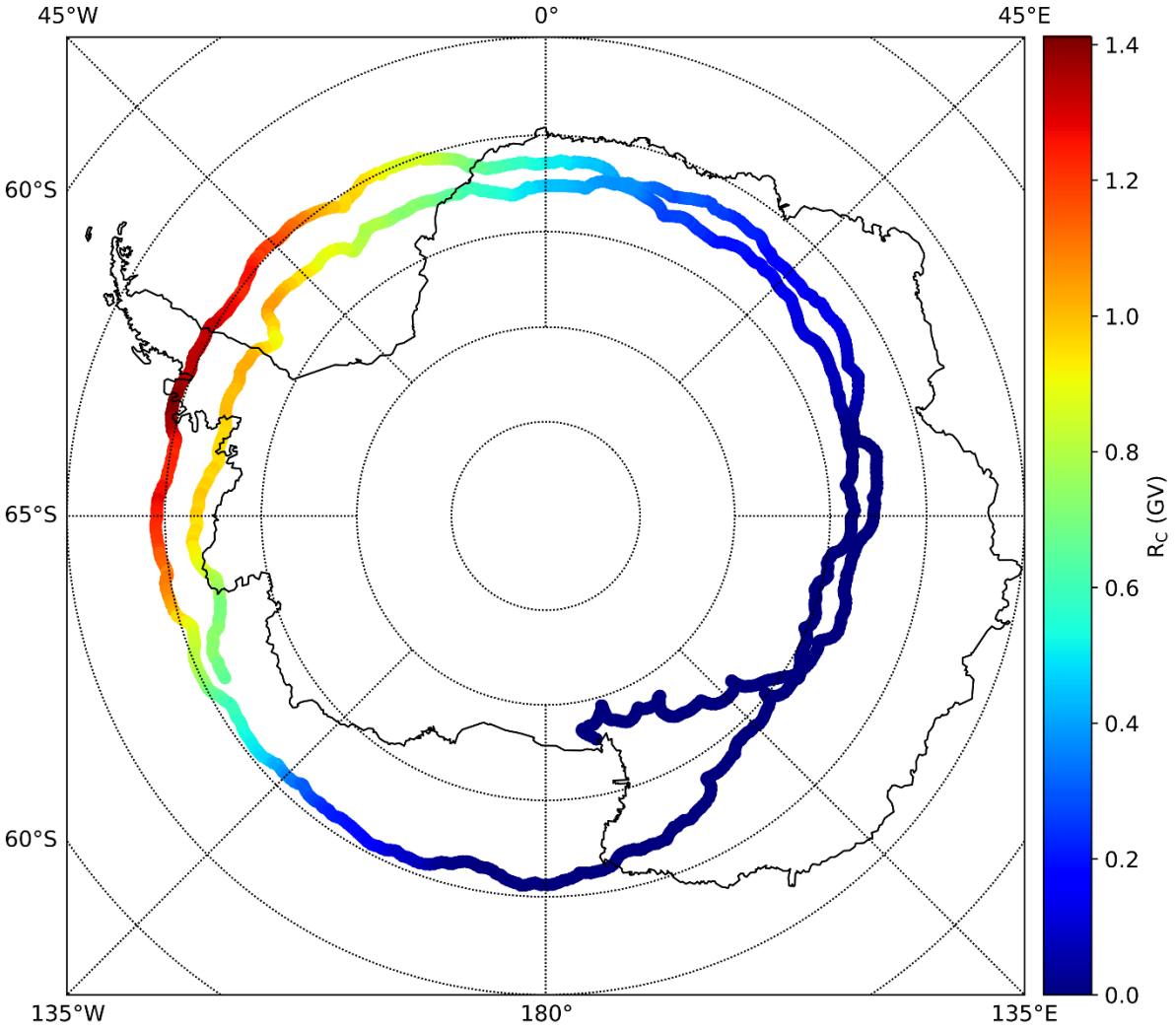

Figure A4. The cut-off rigidity (R_C) over the E-MIST mission.

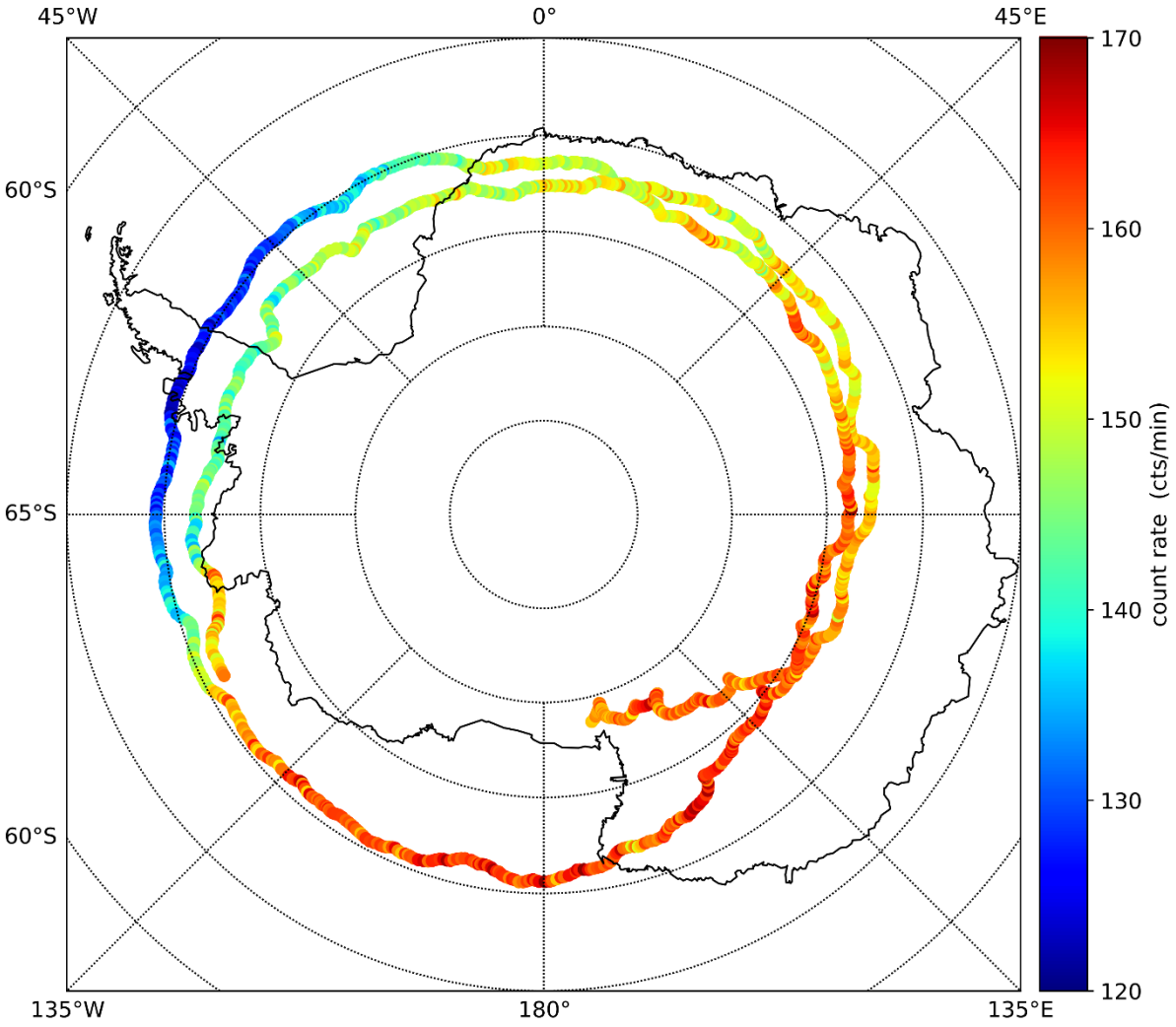

Figure A5. The measured count rate profile (cts/min) over the E-MIST mission. Note: Data refers to the *clean + interpolated* count rate profile as given in Figure 6e.

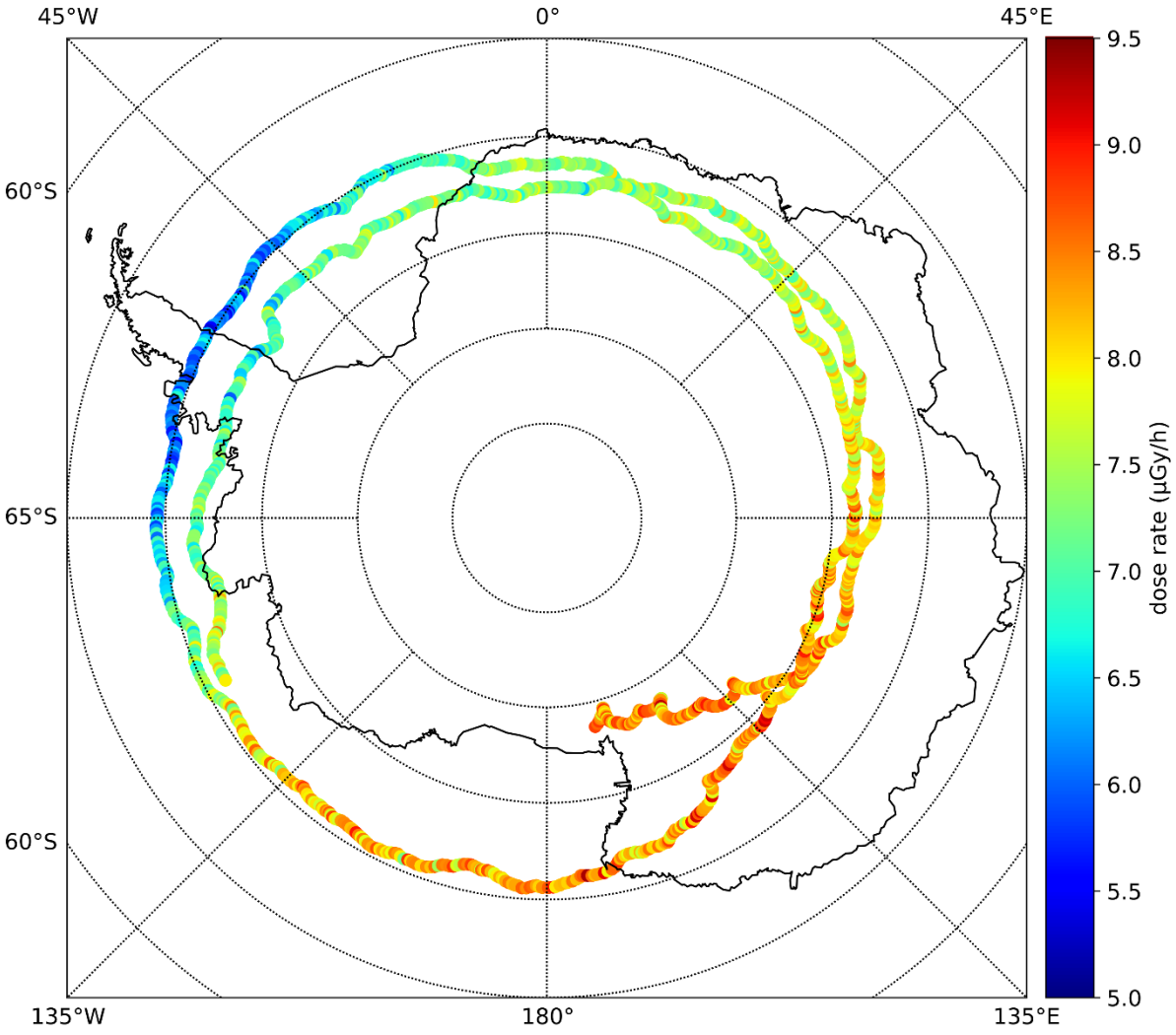

Figure A6. The measured dose rate profile (µGy/h) for the E-MIST mission. Note: Data refers to the *clean + interpolated* dose rate profile as given in Figure 6f and Figure 13b.

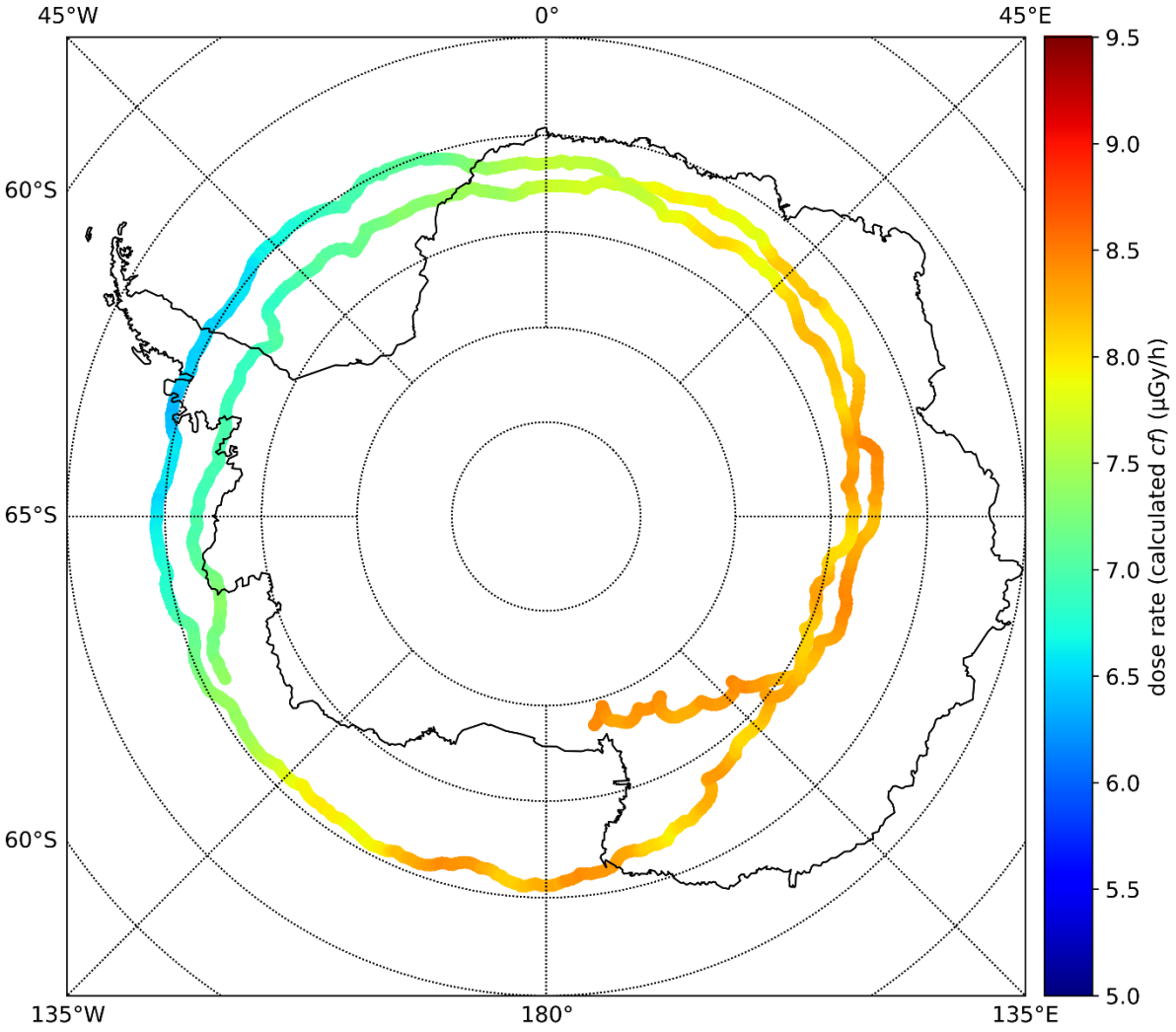

Figure A7. The simulated dose rate profile (µGy/h) for the E-MIST mission with the applied correction factors (*cf*) for R_C and altitude dependence as given in Figure 13b (orange dotted line). Note: Data shown for comparison with the measured dose rate data as given in Figure A6.

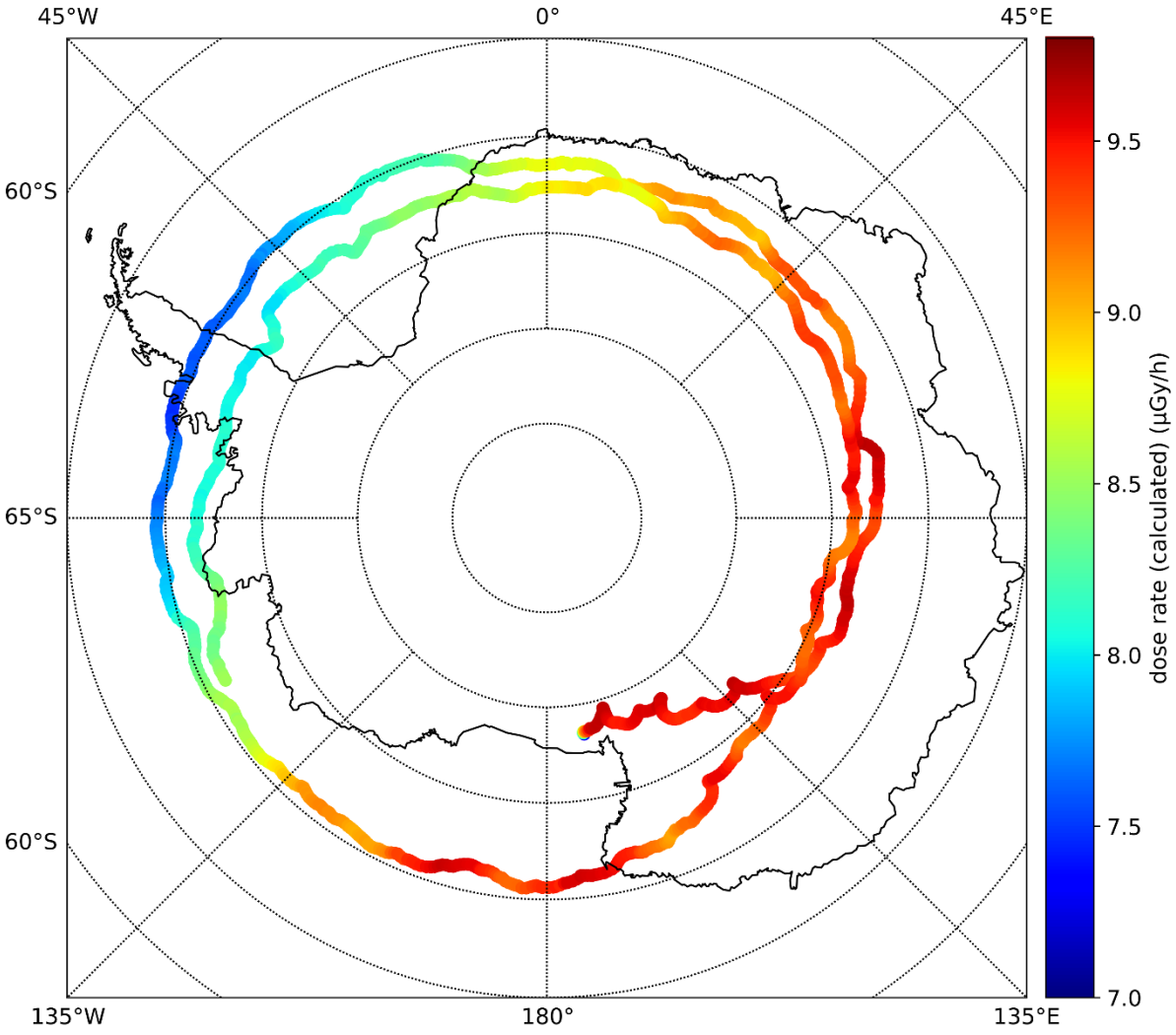

Figure A8. The simulated dose rate profile (µGy/h) for the E-MIST mission as given in Figure 13b (orange dashed line).

Acknowledgments

At DLR, Cologne, DLR M-42 was supported by the DLR grant FuE-Projekt ‘‘OrionRAD” (Programm RF-FuW, Teilprogramm 475).

We would like to thank the NASA Balloon Program Office (BPO), Wallops Flight Facility (WFF), and the staff at the Columbia Scientific Balloon Facility (CSBF), especially Chris Field, Robert Salter and Hugo Franco for flight activities from Fort Sumner, New Mexico, and Antarctica. For the Antarctic mission, our experiment was enabled through the generosity of the SuperTIGER-2.3 team at Washington University in St. Louis (WUSTL); in particular, we express gratitude to Richard Bose, Dana Braun, and Garry Simburger. SuperTIGER-2.3 was funded by NASA grants NNX15AC23G and 80NSSC20K0405. Extensive logistical support for the polar mission was provided by a NASA/National Science Foundation (NSF) agreement supporting awards A-454-M and A-142-M through the United States Antarctic Program’s Antarctic Support Contractor (ASC) at the Long-Duration Balloon (LDB) Facility. We wish to thank Kaija Webster and Scott Battaion (CSBF) from ASC for arranging Antarctic mission activities including post-flight recovery. NASA payloads and team members described herein were funded through balloon research grants from NASA Planetary Protection Research (PPR) and NASA Space Biology.

Data Availability Statement

The data for the sun spot number was obtained from http://www.sidc.be/silso/. Oulu Neutron Monitor (NM) count rate data is provided at https://cosmicrays.oulu.fi/. The values of the *Kp* index were retrieved from ftp://ftp.gfz-potsdam.de/pub/home/obs/kp-ap/. ACE data was retrieved from ftp://ftp.swpc.noaa.gov/pub/lists/ace/.

For the purpose of peer review the data used to generate all figures within the manuscript is provided under the following link for downlink:
https://gigamove.rz.rwth-aachen.de/d/id/YpD8GDJPpNVxRD?20&id=YpD8GDJPpNVxRD

For the purpose of peer review the data used to generate the animated movies within the supplementary material is provided under the following link for downlink:
https://gigamove.rz.rwth-aachen.de/d/id/ELnt5HjgpJKMe6?24&id=ELnt5HjgpJKMe6

Data used to generate all figures and movies of the supplementary material within the manuscript will be made available under the DLR repository at https://zenodo.org.

References

Agostinelli, S., Allison, J., Amako, K. A., Apostolakis, J., Araujo, H. et al. (2003). GEANT4-a simulation toolkit. *Nuclear Instruments and Methods in Physics Research Section A: Accelerators Spectrometers Detectors and Associated Equipment, 506*(3), 250-303. https://doi.org/10.1016/S0168-9002(03)01368-8

Allison, J., Amako, K., Apostolakis, J. E. A., Araujo, H., Dubois, P., Asai, M., et al. (2006). Geant4 developments and applications. *IEEE Transactions on Nuclear Science, 53,* 270-278. https://doi.org/10.1109/TNS.2006.869826

Allison, J., Amako, K., Apostolakis, J., Arce, P., Asai, M., et al. (2016). Recent developments in GEANT4. *Nuclear Instruments and Methods in Physics Research Section A: Accelerators Spectrometers Detectors and Associated Equipment, 835,* 186-225. https://doi.org/10.1016/j.nima.2016.06.125

Bellotti, R., Cafagna, F., Circella, M., De Marzo, C. N., Golden, R. L., Stochaj, S. J. et al. (1999). Balloon measurements of cosmic ray muon spectra in the atmosphere along with those of primary protons and helium nuclei over midlatitude. *Physical Review D, 60*(5), 052002. https://doi.org/10.1103/PhysRevD.60.052002

Berger, T., Marsalek, K., Aeckerlein, J., Hauslage, J., Matthiä, D., Przybyla. B. et al. (2019). The German Aerospace Center M-42 radiation detector – a new development for applications in mixed radiation fields. *Review of Scientific Instruments, 90,* 125115. https://doi.org/10.1063/1.5122301

Berger, T., Matthiä, D., Burmeister, S., Zeitlin, C., Rios, R., Stoffle, N. et al. (2020). Long term variations of galactic cosmic radiation on board the International Space Station, on the Moon and on the surface of Mars. *Journal of Space Weather and Space Climate, 10,* 34. https://doi.org/10.1051/swsc/2020028

Binns, W.R., Bose, R.G., Braun, D.L., Brandt, T.J., Daniels, W.M., De Nolfo, G.A. et al. (2013). *The Super-TIGER Experiment.* Paper presented at the 33rd International Cosmic Ray Conference, 02 – 09 July, 2013, Rio de Janeiro, Brasil. Retrieved from: https://galprop.stanford.edu/elibrary/icrc/2013/papers/icrc2013-0645.pdf

Boezio, M., Carlson, P., Francke, T., Weber, N., Suffert, M., Hof, M., et al. (1999). The Cosmic-Ray Proton and Helium Spectra between 0.4 and 200 GV. *The Astrophysical Journal, 518*(1), 457-472. https://doi.org/10.1086/307251

Boezio, M., Carlson, P., Francke, T., Weber, N., Suffert, M., Hof, M. et al. (2000). The cosmic-ray electron and positron spectra measured at 1 AU during solar minimum activity. *The Astrophysical Journal, 532*(1), 653. https://doi.org/10.1086/308545/

Carlson, P., & Watson, A.A. (2014). Erich Regener and the ionization maximum of the atmosphere. *History of Geo- and Space Sciences, 5,* 175-182. https://doi.org/10.5194/hgss-5-175-2014

Carmichael, H., & Dymond, E. G. (1939). High altitude cosmic radiation measurements near the north geomagnetic pole. *Proceedings of the Royal Society A, 171(946),* 321-344. https://doi.org/10.1098/rspa.1939.0069

Cortesão, M., Siems, L., Koch, S., Beblo-Vranesevic, K., Rabbow, E., Berger, T. et al. (2020). MARSBOx: Fungal and bacterial endurance from a balloon-flown analog mission in the stratosphere. *Frontiers in Microbiology, 12,* 601713. https://doi.org/10.3389/fmicb.2021.601713

DuVernois, M. A., Barwick, S. W., Beatty, J. J., Bhattacharyya, A., Bower, C. R., Chaput, C. J. et al. (2001). Cosmic-Ray Electrons and Positrons from 1 to 100 GeV: Measurements with HEAT and Their Interpretation. *The Astrophysical Journal, 559*(1), 296-303. https://doi.org/10.1086/322324

Goldhagen, P., Clem, J., & Wilson, J. (2004). The energy spectrum of cosmic-ray induced neutrons measured on an airplane over a wide range of altitude and latitude. *Radiation Protection Dosimetry, 110*(1-4), 387-392. https://doi.org/10.1093/rpd/nch216

Grieder, P. K. (2001). Cosmic Rays at Earth. Elsevier. 27 July 2001, ISBN 9780444507105

Hams, T., Binns, W.R. Bose, R.G., Braun D.K, Brandt, T.J., Daniels, W.M., et al. (2016). *SuperTIGER and the Origin of Galactic Cosmic Rays.* Paper presented at the 34th International Cosmic Ray Conference, 30 July - 6 August, 2015, The Hague, The Netherlands. https://doi.org/10.22323/1.236.0435

Hands, A. D. P., Ryden, K.A. and C. J. Mertens C.J. (2016). The disappearance of the pfotzer-regener maximum in dose equivalent measurements in the stratosphere. *Space Weather, 14,* 776–785. https://doi.org/10.1002/2016SW001402

Hauslage, J., Strauch, S.M., Eßmann, O., Haag, F.W.M., Richter, P., Kruger, J., et al. (2018). Eu:CROPIS – "*Euglena gracilis:* Combined Regenerative Organic-food Production in Space" - A Space Experiment Testing Biological Life Support Systems Under Lunar And Martian Gravity. *Microgravity-Science and Technology, 30,* 933-942. https://doi.org/10.1007/s12217-018-9654-1

Khodadad, C.L., Wong, G.M., James, L.M., Thakrar, P.J., Lane, M.A., Catechis, J.A., Smith, D.J. (2017). Stratosphere conditions inactivate bacterial endospores from a Mars spacecraft assembly facility. *Astrobiology, 17*(4), 337-350. https://doi.org/10.1089/ast.2016.1549

Lowder, W. M., & Beck, H. L. (1966). Cosmic-ray ionization in the lower atmosphere. *Journal of Geophysical Research 71*(19), 4661-4668. https://doi.org/10.1029/JZ071i019p04661

Lowder, W. M., Zraft, P. D., & Beck, H. L. (1972). Experimental determination of cosmic ray charged particle intensity profiles in the atmosphere. In: *Proceedings of the National Symposium on Natural and Manmade Radiation in Space, Las Vegas, Nevada*. Retrieved from: https://ntrs.nasa.gov/api/citations/19720010073/downloads/19720010073.pdf

Matthiä, D., Berger, T., Mrigakshi, A.I., and Reitz, G. (2013). A ready-to-use galactic cosmic ray model. *Advances in Space Research, 51,* 329-338. https://doi.org/10.1016/j.asr.2012.09.022

Matthiä, D., & Berger, T. (2017). The radiation environment on the surface of Mars – Numerical calculations of the galactic component with GEANT4/PLANETOCOSMICS. *Life Sciences in Space Research, 14,* 57-63. https://doi.org/10.1016/j.lssr.2017.03.005

Matthiä, D., Hassler, D. M., de Wet, W., Ehresmann, B., Firan, A., Flores-McLaughlin, J., et al. (2017). The radiation environment on the surface of Mars - Summary of model calculations and comparison to RAD data. *Life Sciences in Space Research, 14,* 18-28. https://doi.org/10.1016/j.lssr.2017.06.003

Meier, M. M., Matthiä, D., Forkert, T., Wirtz, M., Scheibinger, M., Hübel, R., and Mertens, C. J. (2016). RaD-X: Complementary measurements of dose rates at aviation altitudes. *Space Weather, 14,* 689-694. https://doi.org/10.1002/2016SW001418

Mertens, C. J. (2016). Overview of the Radiation Dosimetry Experiment (RaD-X) flight mission. *Space Weather, 14,* 921–934. https://doi.org/10.1002/2016SW001399

Mertens, C. J., Gronoff, G. P., Norman, R. B., Hayes, B. M., Lusby, T. C., Straume, T. et al. (2016). Cosmic radiation dose measurements from the RaD-X flight campaign. *Space Weather, 14,* 874–898. https://doi.org/10.1002/2016SW001407

Norman, R. B., C. J. Mertens, andT. C. Slaba (2016). Evaluating galactic cosmic ray environment models using RaD-X flight data. *Space Weather, 14,* 764–775. https://doi.org/10.1002/2016SW001401

Neher, H. V. (1958). The Primary Cosmic Radiation. *Annual Review of Nuclear and Particle Science, 8*(1), 217-242. https://doi.org/10.1146/annurev.ns.08.120158.001245

Neher, H. V. (1971). Cosmic rays at high latitudes and altitudes covering four solar maxima. *Journal of Geophysical Research, 76*(7), 1637-1651.https://doi.org/10.1029/JA076i007p01637

Picone, J. M., Hedin, A. E., Drob, D. P., and Aikin, A. C. (2002). NRLMSISE-00 empirical model of the atmosphere: Statistical comparisons and scientific issues. *Journal of Geophysical Research, 107,* A12, 1468. https://doi.org/10.1029/2002ja009430

Rauch, B. F., Bose, R. G., West, A. T., Lisalda, T., Abarr, Q. et al. (2019). *SuperTIGER-2 2018 Flight Payload Recovery and Preliminary Instrument Assessment*. Paper presented at 36th International Cosmic Ray Conference, 24 July – 01 August 2019, Madison, USA. Retrieved from: https://authors.library.caltech.edu/98062/1/ICRC2019_131.pdf

Regener, E., & Pfotzer, G. (1935). Vertical Intensity of Cosmic Rays by Threefold Coincidences in the Stratosphere. *Nature, 136,* 718–719. https://doi.org/10.1038/136718a0

Rosen, J. M., Hofmann, D. J., & Gringel, W. (1985). Measurements of ion mobility to 30 km. *Journal of Geophysical Research Atmospheres, 90(D4),* 5876-5884. https://doi.org/10.1029/JD090iD04p05876

Smith, D. J., Thakrar, P. J., Bharrat, A. E., Dokos, A. G., Kinney, T. L., James, L. M. et al. (2014). A balloon-based payload for Exposing Microorganisms in the Stratosphere (E-MIST). *Gravitational and Space Research 2,* 70–80.

Straume, T., Mertens, C.J., Lusby, T.C., Gersey, B., Tobiska, W.K., Norman, R.B. et al. (2016). Ground-based evaluation of dosimetersfor NASA high-altitude balloon flight. *Space Weather, 14*, 1011–1025. https://doi.org/10.1002/2016SW001406

Thébault, E., Finlay, C.C., Beggan, C.D., Alken, P., Aubert, J., Barrois, O., et al. (2015). International geomagnetic reference field: the 12th generation. *Earth, Planets and Space, 67*(1), 79. https://doi.org/10.1186/s40623-015-0228-9

Zeitlin, C., Hassler, D., Ehresmann, B., Matthiä, D., Rafkin, S., Berger, T., et al. (2019). Measurements of Radiation Quality Factor on Mars with the Mars Science Laboratory Radiation Assessment Detector. *Life Sciences in Space Research, 22,* 89-97. https://doi.org/10.1016/j.lssr.2019.07.010

Zhang, S., Wimmer-Schweingruber, R.F., Yu, J., Wang, C., Fu, Q., Zou, Y. et al. (2020). First measurements of the radiation dose on the lunar surface. *Science Advances, 6,* eaaz1334. https://doi.org/10.1126/sciadv.aaz1334

1250